Quantifying the minerals abundances on planetary surfaces using VIS–NIR spectroscopy, what uncertainties should we expect? General results and application to the case of phyllosilicates and carbonates on Mars

C. Pilorget, J. Fernando

Quantifying the minerals abundances on planetary surfaces using VIS-NIR spectroscopy, what uncertainties should we expect? General results and application to the case of phyllosilicates and carbonates on Mars.

C. Pilorget[a,*], J. Fernando[b]

[a] *Institut d'Astrophysique Spatiale, Université Paris-Saclay, CNRS, Orsay 91405, France*
[b] *Independent scholar, Orsay 91400, France*

Abstract

Over the last few decades, visible and near-infrared spectroscopy has proven to be an efficient technique to characterize planetary surface mineralogy, in particular thanks to the presence of diagnostic features appropriate for the identification of most minerals of interest. A more quantitative analysis of the VIS-NIR reflectance spectra constitutes the next major step in understanding the planetary bodies' history as the retrieval of the mineral assemblages and their relative abundances enables to constrain the chemical and physical conditions of their formation and, thus, the past and present geologic and climatic processes.

Here, we evaluate the capability to retrieve quantitative properties (abundance, grain size) of intimately mixed materials (the most common mineral mixture among planetary surfaces) from typical space VIS-NIR reflectance spectroscopic data. Such results are key to correctly assess the accuracy and relevance of the retrieved mineral information. For that purpose, we developed an inversion model based on a Monte-Carlo Markov Chains (MCMC) scheme with a Bayesian approach to invert VIS-NIR spectra. This approach allows to properly propagate the uncertainties from the data to the retrieved properties, and finally assess what such uncertainties imply for the interpretation. Different binary and ternary mixtures with minerals of interest in planetary sciences and displaying a large variety of albedos and spectral features were tested. Typical uncertainties, both for the abundance and the grain size, were derived and sensitivities on specific parameters/trends were identified. In particular, the role of absorption features in the spectra is quantified. Tests were performed using either the Hapke or the Shkuratov radiative

transfer model. The case of unidentified endmembers in the mixture is also discussed. In particular, results show that if the unidentified phase does not display any significant spectral feature, the lack of knowledge about its optical properties does not significantly impact the inversion. These different results will be key in the quantitative analyses of VIS-NIR spectra from planetary bodies.

Finally, we analyze more specifically the case of phyllosilicates and carbonates, two families of minerals of high importance in understanding the Mars geologic and climate history. Typical uncertainties on their relative abundances and grain sizes are derived in various cases, providing a critical supporting dataset for the characterization of the martian mineralogy and the associated geological processes.

Keywords: Mineralogy, abundances, spectroscopy, modeling, Mars

---

☆A proposed running head: Uncertainties on mineral abundances estimations

*Corresponding author. Tel.: +33(0)169858732. E-mail address: cedric.pilorget@ias.u-psud.fr

Email addresses: cedric.pilorget@ias.u-psud.fr (C. Pilorget), jfernando.consulting@gmail.com (J. Fernando)

1. Introduction

Over the last few decades, remote sensing reflectance spectroscopy has demonstrated to be an effective technique to assess the surface mineralogical composition of Solar System objects. Particularly, the visible and near-infrared (VIS-NIR) part of the spectrum - typically 0.4-2.5 microns has been used and has proven to be appropriate for the identification of most silicates (e.g., olivines, pyroxenes, phyllosilicates), salts (e.g., carbonates, sulfates), oxides, and ices. Qualitative interpretation of the VIS-NIR reflectance spectra enables so far to access what minerals/ices/organics are present, map them at regional and global scales and determine the major and global processes that occurred on the planetary body (e.g. McCord et al. (1998); Bibring et al. (2006); Kitazato et al. (2019); Nozette et al. (1994)).

A more quantitative analysis of the VIS-NIR reflectance spectra is the next major step in understanding body history. Retrieving the mineral assemblages and their relative abundances enable to constrain the chemical and physical conditions of their formation and their geological settings. For example, on Mars, knowing the olivine composition and its relative abundance enables to directly derive the physical conditions (i.e. temperature and pressure) of the martian mantle (e.g. Ody et al. (2013)). Additionally, deriving the abundance of phyllosilicates, that can only form in an aqueous environment, will support constraining the environmental conditions and assessing the past habitability of Mars (e.g. Poulet et al. (2014)). On the Moon, identifying the minerals abundances enables to characterize the Lunar crustal structure and compositional variation with space and depth to better constrain its evolution and the "magma ocean" hypothesis (e.g., Warren (1985)).

To estimate mineral abundances from the VIS-NIR reflectance spectra, several approaches have been developed: radiative transfer (RT) nonlinear mixture models (e.g. Mustard and Pieters (1987); Shkuratov et al. (1999); Douté et al. (2007); Poulet et al. (2009); Lapotre et al. (2017); Riu et al. (2019)), modified Gaussian models (e.g. Sunshine and Pieters (1993); Noble et al. (2006); Clenet et al. (2013)), RT models in conjunction with statistical analysis such as principal components analysis (e.g. Smith et al. (1985)). Among them, RT approaches (e.g.Hapke (1981, 1984, 1986); Douté and Schmitt (1998); Shkuratov et al. (1999)) are commonly used to determine the mineral abundances from

VIS-NIR data. They are applied to simulate spectra assuming a specific composition (endmembers, grain sizes, abundances), which are then compared to the one that one wants to invert and which serves as a reference. A specific algorithm is generally used to converge towards a solution that tries to fit the simulated spectra with the reference one. Criteria to assess the reliability of the solution usually assumes a chi-square minimization over the entire spectral range or specific areas, sometimes with various weights. However, if a minimum can be found, one can generally not assess if it is a global or just a local minimum. The uncertainty of the solution is also generally not properly assessed (i.e., by propagating the uncertainty on the data).

Here, the capability to retrieve quantitative properties of mineral mixtures (abundance, grain size) from typical space VIS-NIR reflectance spectroscopic data is explored. As remotely sensed surfaces are commonly composed of assemblages of fine-grained intimately mixed minerals, we decided to focus on intimate mixtures in the present study. For that purpose, we developed a model based on a Monte-Carlo Markov Chains (MCMC) scheme with a Bayesian approach to invert VIS-NIR spectra of various compositions. Coupled to a radiative transfer model like the Hapke or Shkuratov model, and assuming a given uncertainty on the data, we can quantitatively evaluate how this uncertainty is propagated to the retrieved parameters and what it implies for their interpretation. Such approach was also used by Lapotre et al. (2017) with the Hapke model to investigate the case of olivine-enstatite-anorthite and olivine-nontronite-basaltic glass ternary mixtures.

Here, we explore various mineral mixtures as well as inversion assumptions with the objective to better understand what controls the uncertainties on the quantitative parameters. First, we characterize the sensitivity of a mixture spectrum to a variation of the fraction and/or grain size of one of the endmembers (Section 3). Then, two- and three- endmember mixtures of minerals of interest are analyzed in Sections 4 and 5. The case of mixtures with some unidentified endmembers is discussed in Section 6. Finally, we examine in Section 7 the case of the phyllosilicates and carbonates on Mars, minerals of critical importance to understand the climate evolution of the planet.

2. Methodology

2.1. Samples

Intimate mixtures of different compositions (2 or 3 endmembers with various grains sizes and abundances) were tested using the Hapke and Shkuratov models. Endmembers include:

- Mg-rich olivine/forsterite (OLV),
- Fe-rich smectite/nontronite (NG1),
- basalt (BAS),
- basaltic glass (BasGl),
- Mg-rich carbonate/magnesite (MGC),

which represent various minerals families (silicates, phyllosilicates, salts) and have diverse spectral properties (overall reflectance, absorption features with different shapes/depths, see Fig.1), all relevant to planetary surfaces. Those 5 endmembers have been selected as they were all well-characterized and used in previous studies (e.g., Ehlmann (2010); Pilorget et al. (2016)). Their description is available in Pilorget et al. (2016).

[Figure 1 about here.]

2.2. Optical constants

The optical constants are defined as follows: $n(\lambda) + i.k(\lambda)$, where n is the real part of the complex refraction index and k the imaginary part. The coefficient $k(\lambda)$ was derived for each endmember using Pilorget et al. (2016) results, more specifically from the single scattering albedo (from the Hapke theory) obtained on pure granular samples previously sieved between 45 and 75 microns, assuming a constant value of n over the spectral range (Fig.2). Usually, the absorptivity of a particle is characterized by its absorption coefficient α, derived from the optical constants as follows (Hapke, 2012):

$$\alpha(\lambda) = \frac{4\pi k}{\lambda} \tag{1}$$

[Figure 2 about here.]

2.3. Radiative transfer models

2.3.1. Hapke model

The semi-analytical Hapke radiative transfer model (Hapke, 1981, 1984, 1986, 2002, 2008) is used to calculate the surface reflectance factor $REFF(i, e, \phi)$ of a semi-infinite granular medium, with particles large compared to the wavelength λ, where i is the incidence angle, e the emergence angle and ϕ the phase angle. The reflectance factor is linked to the bidirectional reflectance as follows:

$$REFF(i, e, \phi) = r(i, e, \phi)\frac{\pi}{\mu_0} \tag{2}$$

with $r(i, e, \phi)$ the bidirectional reflectance and $\mu_0 = cos(i)$.

The model depends on six parameters: the single scattering albedo (which depends on the complex refraction index and the mean grain size), two parameters describing the grain phase function (assuming a 2-lobe Henyey-Greenstein phase function), one parameter related to the surface macroscopic roughness, and two parameters describing the opposition effect). More recently, a new parameter has also been added to simulate the impact of porosity (Hapke, 2008).

The derivation of $REFF(i, e, \phi)$ in the case of an intimate mixture follows three steps:

1. Calculation, for each endmember, of the single scattering albedo ω. Their estimation is done independently of the equations used to solve the radiative transfer. The parameter ω is defined as the ratio of scattered light at the grain scale to extincted light and varies from 0 (the light is totally absorbed) to 1 (the light is totally scattered). It depends on the grain size and the optical constants.
2. Determination of the single scattering albedo of the mixture. For an intimate mixture, the single scattering albedo is computed as the average single scattering albedo of the different endmembers, weighted by their fraction within the mixture.
3. Calculation of the reflectance factor for the specific geometric set (i, e, ϕ). Here an incidence angle (i) of 30 °, an emission angle (e) of 0 ° and a phase angle (ϕ) of 30 ° are assumed. In this configuration, the opposition effect can be neglected (e.g. Hapke (1986); Mustard and Pieters (1989); Fernando et al. (2013)). As for the particles' phase function, it describes the scattering properties of a particle as a

function of phase angle and is related to the particle texture (shape, roughness, internal structure) (e.g. McGuire and Hapke (1995); Shepard and Helfenstein (2007); Souchon et al. (2011); Pilorget et al. (2016)). Since geological processes that shape planetary surfaces grains are quite diverse, a same component may take different textures and thus different phase functions (Fernando et al., 2016). For that reason and to simplify the analysis, we assume a single "mean" isotropic behavior for all cases. The following model can then be applied (Hapke, 2012):

$$REFF(i, e, \phi) = \frac{\omega}{4(\mu + \mu_0)} \frac{1 + 2\mu_0}{1 + 2\gamma\mu_0} \frac{1 + 2\mu}{1 + 2\gamma\mu} \tag{3}$$

with $\mu_0 = cos(i)$, $\mu = cos(e)$ and $\gamma = \sqrt{1 - \omega}$. This assumption may, however, affect the abundance retrieval on the order of 5-10% according to experiments on a series of laboratory mixtures of igneous rock-forming minerals and of natural soils (Mustard and Pieters, 1987).

2.3.2. Shkuratov model

Similar to the Hapke model, the Shkuratov model (Shkuratov et al., 1999) is used to calculate the albedo of a semi-infinite granular medium, but contrary to the previous one, one assumes here that the phase angle is within a few degrees, meaning that one cannot simulate different geometries. It also relies on fewer parameters: the single scattering albedo and the porosity. A particle phase function is computed in the model based on these parameters and is not required as an input.

The derivation of the albedo in the case of an intimate mixture follows three steps:

1. Calculation, for each endmember, of the fraction of light scattered by a grain into the backward hemisphere (r_b) and into the forward hemisphere (r_f) as a function of the optical constants and grain size.
2. Determination of the radiative properties of the mixture. For an intimate mixture, the average parameters r_b and r_f weighted by their fraction within the mixture are computed.
3. Calculation of the albedo of the mixture. The light propagation is simulated as the propagation through a semi-infinite stack of layers, assuming a given porosity. Here, a porosity of 50% is assumed.

2.4. Inversion model

To estimate the relative fraction and grain size (diameter) of each endmember of the mixture, we adapted the procedure developed by Fernando et al. (2013, 2015). This methodology uses a Bayesian approach and was initially applied to determine photometric parameters from the Hapke model.

Fernando et al. (2013, 2015) used the Tarantola and Valette (1982) approach, initally developed to resolve inverse problem for non-linear direct models. The latter is based on the concept of the state of information (e.g. physical domain of a parameter, data uncertainty) characterized by a probability density function (PDF) (e.g. uniform, gaussian). The Bayes theory is used to infer the solution. To numerically sample the final state of information (posterior PDF of each parameter) that corresponds to the solution, Fernando et al. (2013, 2015) used a Monte Carlo Markov Chain (Mosegaard and Tarantola, 1995). Such approach was also followed by Lapotre et al. (2017).

The following hypotheses are applied for the current study:

- Data, model parameters and direct physical model: the direct model F (Hapke or Skuratov model) enables to calculate the data d (reflectance spectrum at a given geometric set) from the model parameters m (fraction and diameter of each endmember within the mixture) such that: $d = F(m)$.

- Prior information about the model parameters m: for a given mixture, the model parameters are the fraction (abundance) and diameter of each component. The prior information is set as a non-nul uniform PDF (named $p(m)$) within the physical domain of the given parameter (fraction from 0 to 1, diameter from 10 to 600 microns here). Outside the physical domain, the PDF is null to avoid any inexistent solution.

- Prior information about the data d: the data is described by a reflectance spectrum from 0.4 to 2.5 μm. Each reflectance factor at a given wavelength is characterized by a value and an uncertainty respectively corresponding to a mean (d_{mes}) and a standard deviation (σ). The prior information is then set as a Gaussian PDF. The data uncertainty at each wavelength is described by a covariance matrix in which

the diagonal contains the variance of the reflectance factor: σ_1^2,..., σ_n^2, with n the n^{th} wavelength.

- Posteriori information about the model parameters: the prior information about model parameters (non-nul uniform PDF) combined with prior information about observations (a Gaussian PDF) are fused to infer the posteriori PDF (named $P(m)$) for each model parameter, by using Bayes theory such as: $P(m) = k.p(m).L(m)$, with k a normalization constant and $L(m)$ the likelihood function used to adjust the observed data (d_{mes}) and the model data (d_{mod}, reflectance factor at each wavelength). The data uncertainty is supposed to be Gaussian with a covariance matrix C. Since the problem is a gaussian linear one (meaning that the prior PDF of the reflectance data has a gaussian form), the likelihood function from Tarantola and Valette (1982) (eq.9-1) is used and is written as:

$$L(m) = exp(-0.5\ (d_{mod} - d_{mes})^T\ C^{-1}\ (d_{mod} - d_{mes})) \quad (4)$$

- Sampling the posteriori PDF (solution chain): as the RT model is non-linear, it is not possible to analytically describe the posterior PDF of each model parameter. Consequently, the posterior PDF is sampled by randomly generating a large collection of model parameter values following the prior PDF from the data and model parameters, and a sampling rule of the solution set by the likelihood function, similar to Mosegaard and Tarantola (1995). Following our tests, after 500 iterations, the state of the solution chain is considered as stationary. These 500 values are considered as a good proxy of the posterior PDF.

This inversion approach enables to get all potential solutions and their likelihood considering a given uncertainty on the data, and thus to retrieve mineral abundances and mean grain sizes from a VIS-NIR reflectance spectrum with their uncertainty (e.g., Fig.3). In what follows, we computed for each distribution the likelihood maximum within the potential solutions of the chain (corresponding to the solution of the inversion), as well as the mean and standard deviation.

[Figure 3 about here.]

3. Sensitivity of a mixture spectrum to fraction and grain size changes

The inversion basically evaluates the sensitivity of the mixture spectrum to a modification of the grain size and the fraction of each endmember (see Figure 4 for example): the larger the effect (integrated over the whole spectral range), the smaller the derived likelihood, assuming a given data uncertainty.

[Figure 4 about here.]

The sensitivity of a mixture spectrum to a modification of the grain size highly depends on the properties of each endmember, more precisely on its absorptivity (cf Eq.1). The evolution of the reflectance factor of a granular sample with the grain size and the absorptivity of the grains was tested (Fig.5a). The sensitivity to a modification of the grain size can be observed as the variation of the reflectance factor around the x-axis (grain size). This sensitivity varies a lot over the tested k and grain size ranges (Fig.5c). In particular, two main areas can be identified: the volume-scattering region (where the overall reflectance factor decreases with increasing k) and the weak-surface-scattering region (where the reflectance factor remains constant with increasing k since all photons that penetrate into a grain are absorbed) (Fig.5b) (Hapke, 2012). The volume-scattering region can be also divided into two domains: the first one where the reflectance factor decreasing rate keeps increasing with increasing k and the second one where the reflectance factor decreasing rate keeps decreasing with increasing k (slowly reaching the weak-surface-scattering region where the decreasing rate is null). The two domains can be observed in Fig.5b on either side of the inflection points of the curves, and in Fig.5c. For example, the presence of an absorption feature (characterized by an increase of k) in the spectrum tends to increase the sensitivity to a modification of the grain size when before this inflection point (above, the sensitivity again decreases). Fig.5 also shows that the smaller the grain size, the smaller the variation of the reflectance factor with k when before the inflection point, and thus the shallower the absorption features, resulting in a smaller impact on the mixture spectrum.

[Figure 5 about here.]

The sensitivity of a mixture spectrum to a modification of the fraction of one of the endmembers also highly depends on the properties of the endmembers (absorptivity)

and their variation over the spectral range. Figure 6 illustrates this sensitivity for diverse binary synthetic mixtures (made of "Endmember 1" and "Endmember 2"). In particular, the variation of the reflectance factor with k is plotted for a fraction of Endmember 1 set to 0.5, 0.6 and 0.7. The difference between the curves illustrates the sensitivity to a modification of the fraction. For instance, it can be observed that when a highly absorbent compound is mixed with a much brighter one, even a small variation of the fraction of the absorbent one has a huge effect on the final reflectance factor (Fig.6a). This effect tends to decrease as the absorptivity of the bright compound tends to increase. On the other hand, when one mixes two bright compounds, the variation of their fraction has very little impact on the final reflectance factor (Fig.6c). These different trends can be explained by the non-linearity of the reflectance with the absorptivity of the different compounds: the absorbent grains tend to control the overall reflectance. As a corollary, when both endmembers have a similar absorptivity, they are not sensitive to a modification of their fraction. Additionally, and similar to what has been observed in Fig.5, the presence of an absorption feature (characterized by an increase of k) in the spectrum, can increase the sensitivity to a modification of the fraction (e.g. Fig.6c). Finally, Fig.6 shows that the smaller the fraction, the shallower the absorption features (obviously), and thus the smaller the impact on the mixture spectrum.

[Figure 6 about here.]

4. Two-endmember mixtures

4.1. Test cases

At first, two-endmember mixtures have been tested. The following endmember combinations have been used:

- nontronite (NG1) + basalt (BAS)
- nontronite (NG1) + basaltic glass (BasGl)
- nontronite (NG1) + olivine (OLV)
- nontronite (NG1) + magnesite (MGC)

- basalt (BAS) + basaltic glass (BasGl)
- olivine (OLV) + magnesite (MGC)

For each couple of endmembers, we tested the following abundances: 10/90%, 20/80%, 30/70%, 40/60%, 50/50%, 60/40%, 70/30%, 80/20% and 90/10%. For each couple and each abundance scenario, we investigated the role of grain size using various diameters between 25 and 500 microns (25, 50, 75, 100, 200, 300, 400, and 500 microns).

The reflectance spectrum of each of the mixtures has been generated using either the Hapke or Shkuratov model. The spectra were then inverted by using the developed inversion model, assuming a data uncertainty of 20% on the reflectance factor. This is typically the order of magnitude that we could expect from space data. In particular, the absolute calibration of near-infrared spectrometers on space missions is generally within 20% (e.g., Bibring et al. (2004)). Uncertainties are also typically related to optical constants, photometric correction, etc.

4.2. Results and interpretation

We can observe the different trends described in Section 3 in the results that we obtained with the different mineral mixtures. The role of the overall reflectance and absorption features, for example, can be illustrated by comparing mixtures of basaltic glass (BasGl) and basalt (BAS), two endmembers that are relatively absorbent with small and broad absorption features ($k \sim 10^{-4} - 7.10^{-4}$), and mixtures of basaltic glass (BasGl) and nontronite (NG1), a brighter compound with strong absorption features ($k \sim 10^{-5} - 5.10^{-4}$). As for the fractions, the standard deviations of the solution distributions are typically around a few percents for the NG1/BasGl while around 10 % for the BAS/BasGl (in absolute) (Fig.7, 8, and 12). In the worst cases (generally small-grained mixtures), the standard deviations can reach values between 10 and 20 % (the worst cases being for the BAS/BasGl mixtures), which means that the quantification of the abundances is poorly constrained (uncertainty of +/- σ, this range containing only 68% of the solutions). For the grain size, its estimation highly depends on the cases (from a few to about 200 microns), with generally smaller uncertainties for the NG1/BasGl mixtures.

[Figure 7 about here.]

[Figure 8 about here.]

[Figure 9 about here.]

[Figure 10 about here.]

Additionally, in the tested cases where one of the endmembers is much more abundant, the grain size of the minor endmember is never well constrained, similar to Lapotre et al. (2017). Indeed, the minor endmember has a small contribution to the mixture spectrum, and the 20% uncertainty on the reflectance data gives a lot of possibilities regarding its grain size. This is typically the case in 10/90% mixtures in Fig.7 where the grain size of the minor endmember can generally take almost any value within the 10-600 microns range.

The uncertainty on the retrieved parameters can have various distributions: more or less pronounced over one or the other dimension (grain size vs. fraction). "Smile" distributions (i.e., distributions where one can see a continuum of solutions from large grains/small fraction to small grains/large fraction for instance), present for various mixtures (e.g., Fig. 9), imply that within the 20% uncertainty on the reflectance data, grain size and fraction can have relatively similar effects. It is, however, not always the case. In some cases, the uncertainty is much more pronounced in one of the two dimensions. For instance, in Fig.7 (NG1/BasGl mixtures), we can notice that for 50/50% mixtures with a similar grain size for both endmembers, the distributions of the solutions vary a lot from one case to the other. When both grain diameters are small (25 microns here), the uncertainty on the retrieved parameters appears much larger over the fraction dimension, while in the case where both grain diameters are large (500 microns here), it appears much larger in the grain size dimension. Generally, when the grain size is larger, the overall reflectance factor is lower and the absorption features are more pronounced. Here, we can observe that the spectrum of large-grained mixture is more sensitive to a modification of the fraction than the grain size (the 20% data uncertainty mostly gives some flexibility on the grain size). However, when the grain size is small, the overall reflectance factor is higher and the absorption features are less pronounced. The spectrum of the mixture, then, is more sensitive to a modification of the grain size (Fig.11).

Other mixtures were also simulated with various endmembers (Mg-rich olivine, basaltic glass, basalt, Fe-rich smectite, and Mg-carbonate) of different grain diameters (from 25 to 500 microns). All fractions from 10/90% to 90/10% with a 10% step have been tested. Standard deviations on both dimensions (fraction and grain size) have been derived, within the assumption of a 20% reflectance factor uncertainty (Fig.12). The standard deviation for the fraction generally lies between a few percents and 15% (in absolute). These values can go up to ∼20-30% when the grain diameter is small (below a few tens of microns in the tested cases) and the absorption features of the mixture spectrum appear relatively shallow. Interestingly, when the fraction is low (<∼10-20%), the uncertainty on the fraction remains small, while the uncertainty on the grain diameter is very high, up to ∼200 microns (i.e. no constraint on the grain diameter). Indeed, since the fraction is small, the absorption features are shallow and a variation of the grain size can easily compensate for a small variation of the fraction, within the 20% data uncertainty. A variation of the grain size can, however, not compensate for a large increase of the fraction, which remains, therefore, well constrained. When the fractions are above ∼10-20%, the standard deviation of the grain diameter generally lies between a few microns and ∼100 microns.

[Figure 11 about here.]

[Figure 12 about here.]

Results obtained with the Hapke and Shkuratov models are quite similar (Fig.13 and Sup. Fig. 1-4). In particular, the retrieved standard deviations for the grain size and the fraction appear to first order equivalent. It can also be noticed that the standard deviations for the grain size can be different for both endmembers within a given mixture, as shown in Fig.13 (left). This difference is similar in both models. These results demonstrate that both models are to first order equally sensitive to a 20% uncertainty on the reflectance data.

[Figure 13 about here.]

A second run of inversion was then performed, assuming this time an uncertainty of 20% on the reflectance data and a relative uncertainty between the spectral channels of

1% (from each spectral channel to the next), similar to the relative calibration that we generally expect on spaceborn VIS-NIR spectrometers. The spectral sampling here is 10 nm. Such case represents a theoretical case since a 1% relative uncertainty may not apply to other contributors (e.g. optical constants). It may, nonetheless, give a good idea on how this constraint can impact the resulting uncertainties on the grain sizes and abundances.

Results show no major variation from the previous case when the absorption features are not too sharp (Fig. 14). However, in the case of mixtures containing nontronite (NG1), the 1% relative uncertainty helps better constraining both the fraction and grain size of the two endmembers. Uncertainties on the fraction, for example, can reach very low values, down to a few percents (Sup. Fig. 5-8). Similar to the previous case, the results obtained with the Hapke and Shkuratov models are quite similar (Fig. 15).

[Figure 14 about here.]

[Figure 15 about here.]

5. Three-endmember mixtures

In this section, three-endmember mixtures are tested. As an example, we consider at first a nontronite (NG1)/olivine (OLV) mixture to which has been added a third endmember ("compound 3"). Its optical constants are as follows: $n + ik$ with $n = 1.5$ and $k = 10^{-2}, 10^{-4}$ or 10^{-6}. Adding this third endmember can have different effects depending on its absorptivity, more specifically on its coefficient k and its grain size, as illustrated in Fig. 16. When the additional endmember is highly absorbent ($k = 10^{-2}$ here), both the continuum and the band depths of the mixture spectrum tend to rapidly decrease as the third endmember is added (Fig.16a). Note that the grain diameter of the third endmember has very little impact on the results: for grain diameters above typically a few tens of microns, all photons that penetrate into the grains are absorbed (i.e. weak-surface-scattering region). This results in a similar absorptivity for these grains. Thus, the grain size of this third endmember cannot be retrieved when mixed with other minerals. To constrain its grain diameter, the absorptivity of these grains has to vary with the grain diameter, typically when the latter is smaller than a few

tens of microns. In the present cases, 25 microns grain size is already quite close to the limit, and the sensitivity to grain size is limited. In most cases, this small effect can be compensated - within the allowed 20% data uncertainty - by playing with the two other endmembers properties (Fig. 17). However, when the additional endmember has a very low absorptivity ($k = 10^{-6}$ here), its impact on the mixture spectrum is limited. Figure 16b shows that the overall reflectance factor tends to increase as the third endmember is added for the tested grain sizes, but the absolute band depths of the features present in the spectra and due to the two other endmembers experience little variation. Neither the fraction nor the grain size can be well constrained for this third compound (Fig.19). Overall, the addition of a third endmember with no or very shallow absorption features tends to increase the relative uncertainties on the retrievals since there is more flexibility in the combination of the different parameters to fit the spectrum within the allowed data uncertainty.

[Figure 16 about here.]

As a second run, 3-endmember mixtures BAS/BasGl/OLV and NG1/OLV/MGC were tested. Results show similar trends as for two-endmember mixtures: both the constraints on the fraction and the grain size depend on the overall absorptivity (through the reflectance) and its variation over the spectral range (i.e., the presence, shape and depth of diagnostic absorption features). The higher the sensitivity of the spectrum to the grain size and the distribution of the abundances, the better the uncertainties on the retrieval (Fig.17,18,19,20, 21, Sup. Fig. 9-13). The uncertainties on the fractions tend to remain relatively similar as for the 2-endmember case (e.g. ∼6% for NG1 in the NG1/MGC and NG1/OLV cases and ∼6% in the NG1/OLV/MGC case, ∼15% for OLV and MGC in the OLV/MGC case and between 12 and 14% in the NG1/OLV/MGC case, ∼10% for BAS and BasGl in the BAS/BasGl case and between 10 and 15% in the BAS/BasGl/OLV case (Fig.12 and 22)). The uncertainties on the grain size tend, however, to be more affected for certain endmembers (e.g. ∼80-90 microns for OLV and MGC in the case of OLV/MGC and respectively ∼120 and ∼160 microns for OLV and MGC in the NG1/OLV/MGC case).

We also tested the case with an additional relative uncertainty (from each spectral channel to the next) of 1% (Fig. 22). As noticed for two-endmember mixtures, results

show no major improvement when only broad absorption bands are present. However, when the spectrum exhibits sharp features, the parameters can be much better constrained (down to a few percents for NG1 abundances for example). As for the previous cases, the results obtained with the Hapke and Shkuratov models are also quite similar.

[Figure 17 about here.]

[Figure 18 about here.]

[Figure 19 about here.]

[Figure 20 about here.]

[Figure 21 about here.]

[Figure 22 about here.]

6. What to expect in case of unidentified endmembers?

In most cases in planetary sciences, some phases remain unidentified, either because they do not display any diagnostic spectral feature in the VIS-NIR spectral range (non-diagnostic spectral features or no spectral features at all if the compound is inactive (e.g., quartz)), or because their fraction is too small and the spectral features remain below the noise level. These phases, however, impact to some extent the mixture spectrum (in particular as a function of the fraction and opacity), and both the continuum and absorption features are affected (e.g., Fig. 16). It is, therefore, not possible to derive the abundances of the identified phases without taking into account these phases.

Their effect can, however, be simulated as an additional compound with specific spectral properties (n and k), similar to "Compound 3" in Section 5. We first simulated a mixture by assuming an unidentified compound which does not display any spectral features (constant n and k in our example) (Fig.23). Results show that the correct abundances (both relative and absolute) and grain sizes of the identified compounds could be efficiently retrieved even though the coefficient k of the unidentified compound had to be assumed with potential bias. Indeed, even though the optical properties of the unidentified compound are not known, the flexibility given by the grain size enables

to converge towards the correct fraction for this endmember. The information about its grain size, however, cannot be derived since it is used here to compensate for the unknown absorptivity of the grains. As long as the unidentified endmember does not display any significant spectral feature, the lack of knowledge about its optical constants will not significantly impact the inversion and the solutions' distribution of the identified endmembers will remain similar. The grain size range for the unidentified endmember shall, nonetheless, be sufficiently broad to give the necessary flexibility.

In the case where the unidentified endmembers display some absorption variations over the spectral range, the identified absorption features will be distorted in an unknown way, which makes impossible the abundances and the grain sizes to be retrieved without any knowledge or assumption about the properties of these unidentified endmembers.

[Figure 23 about here.]

The presence of an additional compound tends to give more flexibility for the identified endmembers, assuming a given uncertainty on the mixture spectrum. How its presence affects the accuracy of the retrieval of the other endmembers parameters depends on their sensitivity to a modification of their fraction and grain size and how they can compensate each other. In the case where the grains of the third endmember are very absorbent ($k = 10^{-2}$ here, shown in Figure 24), the other endmembers are well constrained since the fraction of the third endmember can be easily determined (only a narrow distribution of solutions can explain the overall reflectance factor and bands depths since such high absorptivity has much impact on the mixture spectrum). When the absorptivity of the third endmember decreases (i.e., k decreases), the constraints on the identified endmembers tend to decrease (i.e., broader distribution of the solutions). This, however, does not affect the different endmembers in a similar way as it depends on their own sensitivity to a modification of their fraction/grain size. In the case presented in Fig. 24 where all endmembers have a grain diameter of 250 microns, the nontronite (Endmember 1) is more sensitive than the olivine (Endmember 2), which results in a much better constrained abundance for the nontronite than for the olivine when $k = 10^{-6}$.

When the absorption features of the identified endmembers are shallower, the uncertainty on their abundances tends to increase, as can be seen in Fig. 25. In this

example, the grain diameters of Endmembers 1 and 2 are set to 25 microns (x10 smaller than the previous case, which results in shallower spectral features), while Endmember 3 remains identical (grain diameter of 250 microns). While in the case where $k = 10^{-4}$ and $k = 10^{-6}$, the solutions distributions tend to broaden, the case of $k = 10^{-2}$ is a bit different. In particular, it can be observed that the fraction of Endmember 3 is very well constrained, while solutions found for the fractions of Endmembers 1 and 2 can take a broad range of values between ∼0 and ∼33% (assuming a 20% uncertainty on the data). The fraction of the 3rd compound is, indeed, easily assessed here since it has a huge impact on the mixture spectrum overall reflectance factor due to its high absorptivity compared to the two other endmembers. The relative abundances of the two other compounds, displaying shallow spectral features, are, on the other hand, much more difficult to constrain as the grain size and the fraction can compensate each other within the data uncertainty.

[Figure 24 about here.]

[Figure 25 about here.]

7. Application to the case of phyllosilicates and carbonates on Mars

7.1. Phyllosilicates

VIS-NIR remote sensing data of Mars measured by the Observatoire pour la Minérologie, l'Eau, les Glaces et l'Activité (OMEGA) (Bibring et al., 2004) on board Mars Express and the Compact Reconnaissance Imaging Spectrometer for Mars (CRISM) (Murchie et al., 2007) on board Mars Reconnaissance Orbiter revealed extensive hydrated minerals deposits across the planet. Among them, phyllosilicates could be detected, which completely changed our understanding of the planet's past climate (e.g. Poulet et al. (2005); Bibring et al. (2006). We now know that liquid water was present about 4 billion years ago, either at the surface or in the subsurface, and that conditions favorable for the development of a prebiotic chemistry may have existed. The exact processes that occured on the planet are, however, still unknown, though the mapping and identification of the phyllosilicates on Mars have led to some important constraints (Carter et al., 2013; Ehlmann et al., 2013). The characterization of the mineralogy of the rocks containing

phyllosilicates, and in particular, the quantification of the abundances of the different phases, in their context, will undoubtedly provide important clues to decipher Mars' history and potential prebiotic developments.

Here, we investigate the capability to assess the abundances of nontronite ("NG1", Fe-rich smectite), one of the phyllosilicates detected at the surface of Mars (e.g. Poulet et al. (2005); Ehlmann et al. (2011); Carter et al. (2013); Ehlmann and Edwards (2014)), mixed with a second featureless endmember (e.g. amorphous phase) with various properties.

We assume here a 20% uncertainty on the reflectance data. Figure 26 displays the uncertainties, both on the abundance and the grain size that are obtained for the nontronite. Several properties of the 2^{nd} endmember were tested, from $k = 10^{-6}$ (very transparent) to $k = 10^{-3}$ (very absorbent).

Figure 26 (left column) shows that nontronite abundance can be well constrained, generally within $\sim$5% (1 σ absolute uncertainties) as long as its grain diameter is above $\sim$100μm, though in a few cases where the abundances are low ($\sim$10%) the uncertainties can reach $\sim$10% or more. When its grain diameter is 25μm (black and blue curves), its abundance is much less constrained, especially when the abundance is low. In the latter case, the abundances are basically not constrained because of the very small absorption features in the spectrum, which are in the present case only related to NG1 since the second endmember is featureless. As the abundances increase, the absorption depths increase as well, and the abundance uncertainties decrease, down to $\sim$10% for mixtures with 90% of NG1. The properties of the 2^{nd} endmember do not show any major impact on the results, except that the abundance of NG1 tends to be more constrained as the second endmember is more absorbent. This might seem to be in contradiction with the fact that the signatures tend to lower as the absorptivity of the 2^{nd} endmember increases. The resulting low reflectance factor level, however, provides some important constraints in the inversion.

The uncertainty on the nontronite grain diameter varies a lot from the different cases tested, as shown in Figure 26 (right column). It tends to decrease as the fraction of NG1 increases, similar to what has been observed in Section 4 (basically no or little constraint when the fraction lies within 10%). The uncertainties on the nontronite grain diameter are, however, typically within 50μm when the abundance is above 50%.

Tests were also performed assuming properties of the 2^{nd} endmember different from the real ones (factor of 10 or 0.1 on k) and did not show any significant differences on the uncertainties and solutions retrieved for the grain size and abundance of NG1, in agreement with the results obtained in Section 6.

Properties of nontronite and compounds with close spectral characteristics should thus be relatively well constrained when detected at the surface of Mars, assuming that the spectral model can correctly reproduce the variations, both in grain diameters and abundances of the mixtures encountered on Mars. Compounds with different properties will have to be investigated on a case-by-case basis. In particular, phyllosilicate-rich surfaces may display shallower absorption features compared to terrestrial samples because of different physiochemical properties caused by the pressure and temperature conditions of the Mars environment under which those materials were formed (Morris et al., 2011) and/or the exposure to the current Martian environment (e.g., exposure to UV, low atmospheric pressure) (Cloutis et al., 2007). Future studies will focus on specific Mars cases, taking into account the geological contexts, and including, if relevant, optical constants from more adapted analog samples.

[Figure 26 about here.]

7.2. Carbonates

Given the CO_2-rich Mars atmosphere composition and the widespread near-surface aqueous alteration in its past history, one might expect to detect extensive carbonate deposits on Mars. However, while phyllosilicates have a widespread distribution from VIS-NIR remote sensing data, carbonates show regionally restricted distributions (e.g., (Ehlmann et al., 2008; Ehlmann and Edwards, 2014)).

As for the phyllosilicates, here we explore the capability to assess the abundances of magnesite ("MGC", magnesium-rich carbonate) (e.g., (Bandfield et al., 2003; Ehlmann et al., 2008; Morris et al., 2010)) using the same approach. Figure 27 shows the abundance (left) and grain size (right) uncertainties that are obtained for the magnesite. For the inversion, several properties of the 2^{nd} endmember were tested, from $k = 10^{-6}$ (very transparent) to $k = 10^{-3}$ (very absorbent).

Results show that magnesite abundance can generally not be accurately constrained (Figure 27, left column). In most cases, the uncertainty on the abundance lies above 10%, except (but not in all cases) when the grain diameter of MGC is large (500μm here). The influence of the grain size, thus of the depth of the spectral features, does constrain a lot the possibility to accurately retrieve the abundance of magnesite. For smaller grain sizes, the abundance uncertainties of MGC generally lie between 10 and 35%. Above 15-20%, we can assume that the abundances are not (or only poorly) constrained. Similar to what has been observed for nontronite (see Section 7.1), when the 2^{nd} endmember is highly absorbent ($k = 10^{-2}$ here), the abundance uncertainties tend to decrease and lie within 10% in most cases.

The uncertainties on the grain size vary a lot from the different cases (Fig. 27, right column). They generally tend to decrease as the fraction of MGC increases, similar to what has been previously observed. Only a few cases display uncertainties within $\sim$50μm: cases where we combine a large grain diameter (500μm here) with a large fraction ($\sim$90%), or in a couple of cases when the 2^{nd} endmember is highly absorbent.

Similar to what is presented in Section 7.1, tests were also performed assuming that properties of the 2^{nd} endmember were different from the real ones (factor of 10 and 0.1 on k) and did not show any significant differences in the uncertainties and solutions retrieved for the grain size and abundance of MGC.

Abundances and grain sizes of magnesite thus appear to be generally relatively difficult to constrain, mainly because of its high reflectance factor and relatively small absorption features between 0.4 and 2.6μm. Large grained mixtures, however, tend to display small uncertainties on the abundances. Other carbonate compounds with different properties will have to be investigated on a case-by-case basis.

[Figure 27 about here.]

8. Conclusion

The inversion approach that we have developed enables to get all potential solutions and their likelihood considering a given uncertainty on the data, and thus, to retrieve mineral abundances and mean grain sizes from a VIS-NIR reflectance spectrum with

their uncertainties. Thanks to this model, we have tested various mixtures, displaying a large variety of albedos and spectral features, typical on what can be encountered on planetary surfaces over the VIS-NIR spectral range.

Typical uncertainties, both for the abundance and the grain size, have been derived, and sensitivities on specific parameters/trends have been identified. In particular, we have shown that:

- both the abundances and the grains sizes are better constrained when they have a large impact on the mixture spectrum. For instance, the abundance of a dark endmember among bright ones can be well characterized as these absorbent grains are driving the overall reflectance factor.

- absorption features present in the spectrum of one of the endmembers do not necessarily help to constrain the abundance / grain size. Indeed, the critical parameter is the k range (and values) over the spectrum and the sensitivity of the reflectance factor to this parameter.

- within a given data uncertainty, grain size and fraction can have relatively similar effects, which might lead to difficulties to assess these parameters. In particular, when the fraction of one of the endmembers is small (typically within $\sim$10-20%), the absorption features are shallow, and the grain size can generally not be well constrained, contrary to the abundance.

- for the different tested cases, uncertainties on the abundance (1σ standard deviation of the distribution) generally lie between a few percents and 15% (in absolute). These values can reach $\sim$20-30% when the grain sizes are small (typically within a few tens of microns in the tested cases), and the absorption features appear relatively shallow.

- in most cases in planetary science, some phases remain unidentified. The latter need to be taken into account in the models to derive the abundances of the identified phases. If the unidentified phase does not display any significant spectral feature, it is possible to replace it with an endmember with similar spectral shape and assess the correct abundances (for all endmembers) and grain sizes (except for the unidentified phase), with the uncertainties that such mixture imply .

- all results do not show any significant difference whether the Hapke or Shkuratov model was used.

- the addition of a constraint on the relative uncertainty from one spectral channel to the next (1% here) to the data uncertainty of 20% do not significantly impact the results as long as absorption features remain relatively broad. In the case of sharp absorption bands, their presence can significantly reduce the uncertainties. This, however, remains a theoretical case since it requires the relative uncertainty of all contributors combined to reach 1%.

We finally investigated the case of phyllosilicates (through the example of nontronite) and carbonates (through the example of magnesite), two families of high importance in Mars science. We have derived typical uncertainties (1σ standard deviation) on their relative abundances and grain size that could be expected when inverting reflectance spectra of mixtures made of these compounds and other featureless compounds. Results have shown that nontronite abundances could generally be well constrained (generally within 5%) except when the grain diameter is below a few tens of microns or when the fractions are very low (10%). As for the magnesite, it is much more difficult to characterize: uncertainties on the abundances are typically between 10% and 35% except in some cases where the grains are large (above a few hundreds of microns in diameter) or when mixed with a highly absorbent phase. Such results will be key in the characterization of the martian mineralogy and the associated geological processes.

More generally, models, that are capable to propagate the uncertainties on the data to the endmembers properties (abundances and grain sizes), similar to the one presented in this paper, will be critical in the future to correctly assess the accuracy and relevance of the quantitative information retrieved from VIS-NIR reflectance spectra. Areal and intraparticle mixtures, also observed among planetary surfaces, should also be subject to such kind of evaluation in the future. Future studies will focus on specific cases (e.g., Martian landing sites) and explore new endmembers (e.g., Fe-oxides, pyroxenes) to mimic as possible typical global/regional contexts.

Acknowledgement

We would like to thank our colleagues at IAS for helpful discussions. We are also grateful to the reviewer for its detailed comments and suggestions, as well as the editorial team of Icarus for manuscript preparation and publication.

References

Bandfield, J. L., Glotch, T. D., Christensen, P. R., Aug. 2003. Spectroscopic Identification of Carbonate Minerals in the Martian Dust. Science 301 (5636), 1084–1087.

Bibring, J.-P., Langevin, Y., Mustard, J. F., Poulet, F., Arvidson, R., Gendrin, A., Gondet, B., Mangold, N., Pinet, P., Forget, F., 2006. Global Mineralogical and Aqueous Mars History Derived from OMEGA/Mars Express Data. Science 312, 400–404.

Bibring, J.-P., Soufflot, A., Berthé, M., Langevin, Y., Gondet, B., Drossart, P., Bouyé, M., Combes, M., Puget, P., Semery, A., Bellucci, G., Formisano, V., Moroz, V., Kottsov, V., Bonello, G., Erard, S., Forni, O., Gendrin, A., Manaud, N., Poulet, F., Poulleau, G., Encrenaz, T., Fouchet, T., Melchiori, R., Altieri, F., Ignatiev, N., Titov, D., Zasova, L., Coradini, A., Capacionni, F., Cerroni, P., Fonti, S., Mangold, N., Pinet, P., Schmitt, B., Sotin, C., Hauber, E., Hoffmann, H., Jaumann, R., Keller, U., Arvidson, R., Mustard, J., Forget, F., 2004. OMEGA: Observatoire pour la Minéralogie, l'Eau, les Glaces et l'Activité. ESA SP-1240: Mars Express: the Scientific Payload, pp. 37–49.

Carter, J., Poulet, F., Bibring, J. P., Mangold, N., Murchie, S., Apr 2013. Hydrous minerals on Mars as seen by the CRISM and OMEGA imaging spectrometers: Updated global view. Journal of Geophysical Research (Planets) 118 (4), 831–858.

Clenet, H., Pinet, P., Ceuleneer, G., Daydou, Y., Heuripeau, F., Rosemberg, C., Bibring, J.-P., Bellucci, G., Altieri, F., Gondet, B., Aug. 2013. A systematic mapping procedure based on the Modified Gaussian Model to characterize magmatic units from olivine/pyroxenes mixtures: Application to the Syrtis Major volcanic shield on Mars. Journal of Geophysical Research (Planets) 118 (8), 1632–1655.

Cloutis, E. A., Craig, M. A., Mustard, J. F., Kruzelecky, R. V., Jamroz, W. R., Scott, A., Bish, D. L., Poulet, F., Bibring, J.-P., King, P. L., Oct. 2007. Stability of hydrated minerals on Mars. GRL 34 (20), L20202.

Douté, S., Schmitt, B., Dec. 1998. A multilayer bidirectional reflectance model for the analysis of planetary surface hyperspectral images at visible and near-infrared wavelengths. J. Geophys. Res. 103, 31367–31390.

Douté, S., Schmitt, B., Langevin, Y., Bibring, J. P., Altieri, F., Bellucci, G., Gondet, B., Poulet, F., Mex OMEGA Team, Jan 2007. South Pole of Mars: Nature and composition of the icy terrains from Mars Express OMEGA observations. Planet. Space Sci. 55 (1-2), 113–133.

Ehlmann, B. L., 2010. Early Mars Environments Revealed Through Near Infrared Spectroscopy of Alteration Mineral Assemblages Geological Sciences, PhD thesis.

712 Ehlmann, B. L., Berger, G., Mangold, N., Michalski, J. R., Catling, D. C., Ruff, S. W., Chassefière,
713 E., Niles, P. B., Chevrier, V., Poulet, F., Jan. 2013. Geochemical Consequences of Widespread Clay
714 Mineral Formation in Mars' Ancient Crust. Space Science Reviews 174 (1-4), 329–364.
715 Ehlmann, B. L., Edwards, C. S., May 2014. Mineralogy of the Martian Surface. Annual Review of Earth
716 and Planetary Sciences 42 (1), 291–315.
717 Ehlmann, B. L., Mustard, J. F., Murchie, S. L., Bibring, J.-P., Meunier, A., Fraeman, A. A., Langevin,
718 Y., Nov 2011. Subsurface water and clay mineral formation during the early history of Mars. Nature
719 479 (7371), 53–60.
720 Ehlmann, B. L., Mustard, J. F., Murchie, S. L., Poulet, F., Bishop, J. L., Brown, A. J., Calvin, W. M.,
721 Clark, R. N., Des Marais, D. J., Milliken, R. E., Roach, L. H., Roush, T. L., Swayze, G. A., Wray,
722 J. J., Dec. 2008. Orbital Identification of Carbonate-Bearing Rocks on Mars. Science 322 (5909), 1828.
723 Fernando, J., Schmidt, F., Ceamanos, X., Pinet, P., Douté, S., Daydou, Y., Mar. 2013. Surface reflectance
724 of Mars observed by CRISM/MRO: 2. Estimation of surface photometric properties in Gusev Crater
725 and Meridiani Planum. Journal of Geophysical Research (Planets) 118, 534–559.
726 Fernando, J., Schmidt, F., Douté, S., Sep. 2016. Martian surface microtexture from orbital CRISM
727 multi-angular observations: A new perspective for the characterization of the geological processes.
728 PSS 128, 30–51.
729 Fernando, J., Schmidt, F., Pilorget, C., Pinet, P., Ceamanos, X., Douté, S., Daydou, Y., Costard,
730 F., Jun. 2015. Characterization and mapping of surface physical properties of Mars from CRISM
731 multi-angular data: Application to Gusev Crater and Meridiani Planum. Icarus 253, 271–295.
732 Hapke, B., 1981. Bidirectional reflectance spectroscopy 1. Theory. J. Geophys. Res. 86, 3039–3054.
733 Hapke, B., Jul. 1984. Bidirectional reflectance spectroscopy. III - Correction for macroscopic roughness.
734 Icarus 59, 41–59.
735 Hapke, B., 1986. Bidirectional reflectance spectroscopy 4. The extinction coefficient and the opposition
736 effect. Icarus 67, 264–280.
737 Hapke, B., Jun. 2002. Bidirectional Reflectance Spectroscopy5. The Coherent Backscatter Opposition
738 Effect and Anisotropic Scattering. Icarus 157, 523–534.
739 Hapke, B., Jun. 2008. Bidirectional reflectance spectroscopy. 6. Effects of porosity. Icarus 195, 918–926.
740 Hapke, B., 2012. Theory of reflectance and emittance spectroscopy, Second edition. Cambridge University
741 Press.
742 Kitazato, K., Milliken, R. E., Iwata, T., Abe, M., Ohtake, M., Matsuura, S., Arai, T., Nakauchi, Y.,
743 Nakamura, T., Matsuoka, M., Senshu, H., Hirata, N., Hiroi, T., Pilorget, C., Brunetto, R., Poulet, F.,
744 Riu, L., Bibring, J. P., Takir, D., Domingue, D. L., Vilas, F., Barucci, M. A., Perna, D., Palomba, E.,
745 Galiano, A., Tsumura, K., Osawa, T., Komatsu, M., Nakato, A., Arai, T., Takato, N., Matsunaga,
746 T., Takagi, Y., Matsumoto, K., Kouyama, T., Yokota, Y., Tatsumi, E., Sakatani, N., Yamamoto, Y.,
747 Okada, T., Sugita, S., Honda, R., Morota, T., Kameda, S., Sawada, H., Honda, C., Yamada, M.,
748 Suzuki, H., Yoshioka, K., Hayakawa, M., Ogawa, K., Cho, Y., Shirai, K., Shimaki, Y., Hirata, N.,
749 Yamaguchi, A., Ogawa, N., Terui, F., Yamaguchi, T., Takei, Y., Saiki, T., Nakazawa, S., Tanaka,
750 S., Yoshikawa, M., Watanabe, S., Tsuda, Y., Apr. 2019. The surface composition of asteroid 162173

751 Ryugu from Hayabusa2 near-infrared spectroscopy. Science 364 (6437), 272–275.
752 Lapotre, M. G. A., Ehlmann, B. L., Minson, S. E., May 2017. A probabilistic approach to remote
753 compositional analysis of planetary surfaces. Journal of Geophysical Research (Planets) 122 (5), 983–
754 1009.
755 McCord, T. B., Hansen, G. B., Fanale, F. P., Carlson, R. W., Matson, D. L., Johnson, T. V., Smythe,
756 W. D., Crowley, J. K., Martin, P. D., Ocampo, A., Hibbitts, C. A., Granahan, J. C., May 1998. Salts
757 on Europa's Surface Detected by Galileo's Near Infrared Mapping Spectrometer. Science 280, 1242.
758 McGuire, A. F., Hapke, B. W., Jan. 1995. An experimental study of light scattering by large, irregular
759 particles. Icarus 113, 134–155.
760 Morris, R. V., Graff, T. G., Achilles, C. N., Agresti, D. A., Ming, D. W., Golden, D. C., Mar. 2011.
761 Visible and Near-IR Reflectance Spectra of Mars Analogue Materials Under Arid Conditions for
762 Interpretation of Martian Surface Mineralogy. In: Lunar and Planetary Science Conference. Lunar
763 and Planetary Science Conference. p. 2757.
764 Morris, R. V., Ruff, S. W., Gellert, R., Ming, D. W., Arvidson, R. E., Clark, B. C., Golden, D. C.,
765 Siebach, K., Klingelhöfer, G., Schröder, C., Fleischer, I., Yen, A. S., Squyres, S. W., Jul. 2010.
766 Identification of Carbonate-Rich Outcrops on Mars by the Spirit Rover. Science 329 (5990), 421.
767 Mosegaard, K., Tarantola, A., Jul. 1995. Monte Carlo sampling of solutions to inverse problems. J. Geo-
768 phys. Res. 100, 12431.
769 Murchie, S., Arvidson, R., Bedini, P., Beisser, K., Bibring, J.-P., Bishop, J., Boldt, J., Cavender, P.,
770 Choo, T., Clancy, R. T., Darlington, E. H., Des Marais, D., Espiritu, R., Fort, D., Green, R., Guinness,
771 E., Hayes, J., Hash, C., Heffernan, K., Hemmler, J., Heyler, G., Humm, D., Hutcheson, J., Izenberg,
772 N., Lee, R., Lees, J., Lohr, D., Malaret, E., Martin, T., McGovern, J. A., McGuire, P., Morris, R.,
773 Mustard, J., Pelkey, S., Rhodes, E., Robinson, M., Roush, T., Schaefer, E., Seagrave, G., Seelos,
774 F., Silverglate, P., Slavney, S., Smith, M., Shyong, W.-J., Strohbehn, K., Taylor, H., Thompson, P.,
775 Tossman, B., Wirzburger, M., Wolff, M., 2007. Compact Reconnaissance Imaging Spectrometer for
776 Mars (CRISM) on Mars Reconnaissance Orbiter (MRO). Journal of Geophysical Research (Planets)
777 112 (E11), 5–+.
778 Mustard, J. F., Pieters, C. M., Mar. 1987. Quantitative abundance estimates from bidirectional re-
779 flectance measurements. JGR 92, E617–E626.
780 Mustard, J. F., Pieters, C. M., Oct. 1989. Photometric phase functions of common geologic minerals and
781 applications to quantitative analysis of mineral mixture reflectance spectra. JGR 94, 13619–13634.
782 Noble, S. K., Pieters, C. M., Hiroi, T., Taylor, L. A., Nov. 2006. Using the modified Gaussian model
783 to extract quantitative data from lunar soils. Journal of Geophysical Research (Planets) 111 (E11),
784 E11009.
785 Nozette, S., Rustan, P., Pleasance, L. P., Horan, D. M., Regeon, P., Shoemaker, E. M., Spudis, P. D.,
786 Acton, C. H., Baker, D. N., Blamont, J. E., Buratti, B. J., Corson, M. P., Davies, M. E., Duxbury,
787 T. C., Eliason, E. M., Jakosky, B. M., Kordas, J. F., Lewis, I. T., Lichtenberg, C. L., Lucey, P. G.,
788 Malaret, E., Massie, M. A., Resnick, J. H., Rollins, C. J., Park, H. S., McEwen, A. S., Priest, R. E.,
789 Pieters, C. M., Reisse, R. A., Robinson, M. S., Simpson, R. A., Smith, D. E., Sorenson, T. C., Vorder

Breugge, R. W., Zuber, M. T., Dec. 1994. The Clementine Mission to the Moon: Scientific Overview. Science 266 (5192), 1835–1839.

Ody, A., Poulet, F., Bibring, J. P., Loizeau, D., Carter, J., Gondet, B., Langevin, Y., Feb 2013. Global investigation of olivine on Mars: Insights into crust and mantle compositions. Journal of Geophysical Research (Planets) 118 (2), 234–262.

Pilorget, C., Fernando, J., Ehlmann, B. L., Schmidt, F., Hiroi, T., Mar 2016. Wavelength dependence of scattering properties in the VIS-NIR and links with grain-scale physical and compositional properties. Icarus 267, 296–314.

Poulet, F., Bibring, J.-P., Langevin, Y., Mustard, J. F., Mangold, N., Vincendon, M., Gondet, B., Pinet, P., Bardintzeff, J.-M., Platevoet, B., May 2009. Quantitative compositional analysis of martian mafic regions using the MEx/OMEGA reflectance data 1. Methodology, uncertainties and examples of application. Icarus 201, 69–83.

Poulet, F., Bibring, J.-P., Mustard, J. F., Gendrin, A., Mangold, N., Langevin, Y., Arvidson, R. E., Gondet, B., Gomez, C., Dec. 2005. Phyllosilicates on Mars and implications for early martian climate. Nature 438, 623–627.

Poulet, F., Carter, J., Bishop, J. L., Loizeau, D., Murchie, S. M., Mar. 2014. Mineral abundances at the final four curiosity study sites and implications for their formation. Icarus 231, 65–76.

Riu, L., Poulet, F., Bibring, J. P., Gondet, B., Apr 2019. The M^3 project: 2 - Global distributions of mafic mineral abundances on Mars. Icarus 322, 31–53.

Shepard, M. K., Helfenstein, P., Mar. 2007. A test of the Hapke photometric model. Journal of Geophysical Research (Planets) 112, 3001.

Shkuratov, Y., Starukhina, L., Hoffmann, H., Arnold, G., Feb. 1999. A Model of Spectral Albedo of Particulate Surfaces: Implications for Optical Properties of the Moon. Icarus 137, 235–246.

Smith, M. O., Johnson, P. E., Adams, J. B., Jan. 1985. Quantitative determination of mineral types and abundances from reflectance spectra using principal components analysis. JGR 90, C797–C804.

Souchon, A. L., Pinet, P. C., Chevrel, S. D., Daydou, Y. H., Baratoux, D., Kurita, K., Shepard, M. K., Helfenstein, P., Sep. 2011. An experimental study of Hapke's modeling of natural granular surface samples. Icarus 215, 313–331.

Sunshine, J. M., Pieters, C. M., 1993. Estimating modal abundances from the spectra of natural and laboratory pyroxene mixtures using the modified Gaussian model. J. Geophys. Res. 98, 9075–9087.

Tarantola, A., Valette, B., May 1982. Generalized Nonlinear Inverse Problems Solved Using the Least Squares Criterion (Paper 1R1855). Reviews of Geophysics and Space Physics 20, 219.

Warren, P. H., Jan. 1985. The magma ocean concept and lunar evolution. Annual Review of Earth and Planetary Sciences 13, 201–240.

List of Figures

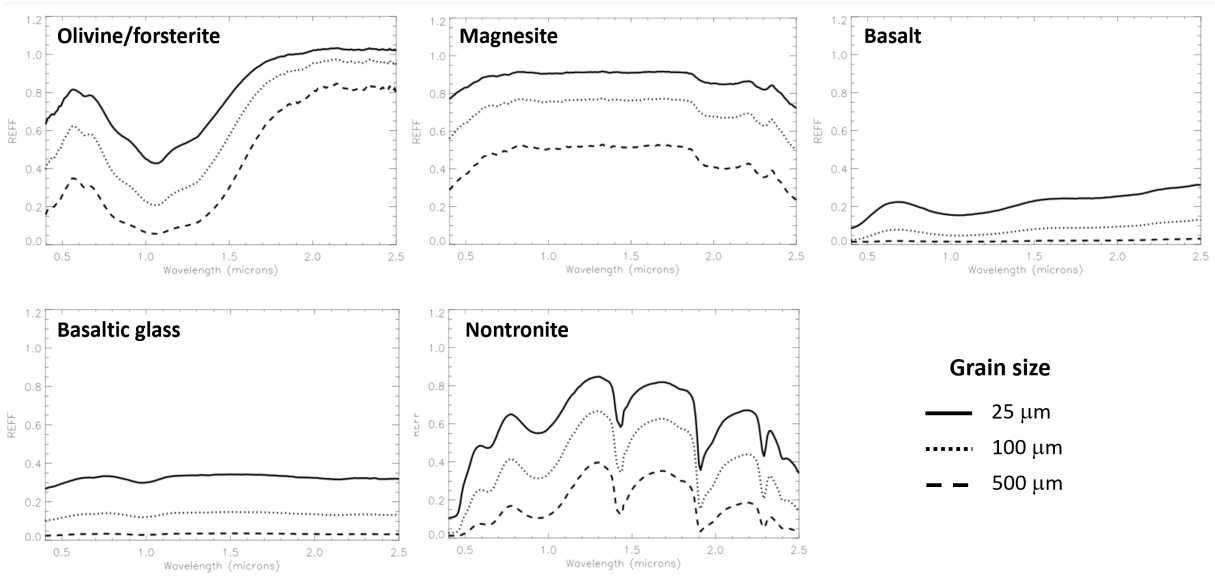

Figure 1: *Reflectance spectra (REFF unit = (I/F)/cos i) of the different endmembers used in this study: olivine/forsterite (OLV), nontronite (NG1), basalt (BAS), basaltic glass (BasGl) and magnesite (MGC). These spectra are simulated with the Hapke model for the following grain diameters: 25, 100, and 500 microns. Optical constants were derived from Pilorget et al. (2016).*

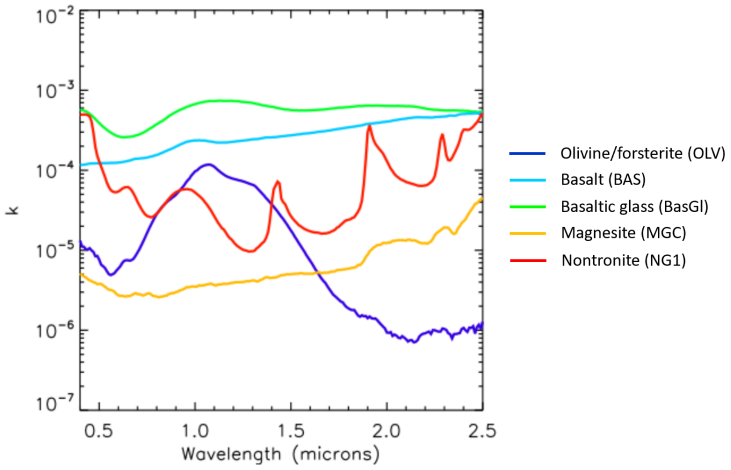

Figure 2: *Imaginary part of the complex refraction index k as a function of the wavelength for the different tested endmembers. Results are derived from Pilorget et al. (2016), assuming a constant real part of the refraction index n over the spectral range ($n = 1.5$ for NG1, $n = 1.6$ for BAS, BasGl, OLV and MGC). The granular samples used to derive k were sieved between 45 and 75 microns.*

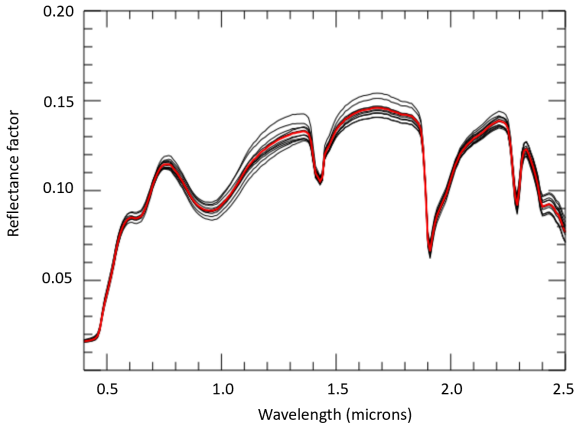

Figure 3: *In red: modeled reflectance spectrum of a 50%/50% mixture of nontronite (NG1) and basaltic glass (BasGl). Grain diameter for both endmembers is set to 200 microns. In black: examples of solutions obtained from the inversion assuming a data uncertainty of 20%. Eleven samples from the Markov chain (equally sampled from the last 500 iterations) are displayed here. The Hapke model is used in this example.*

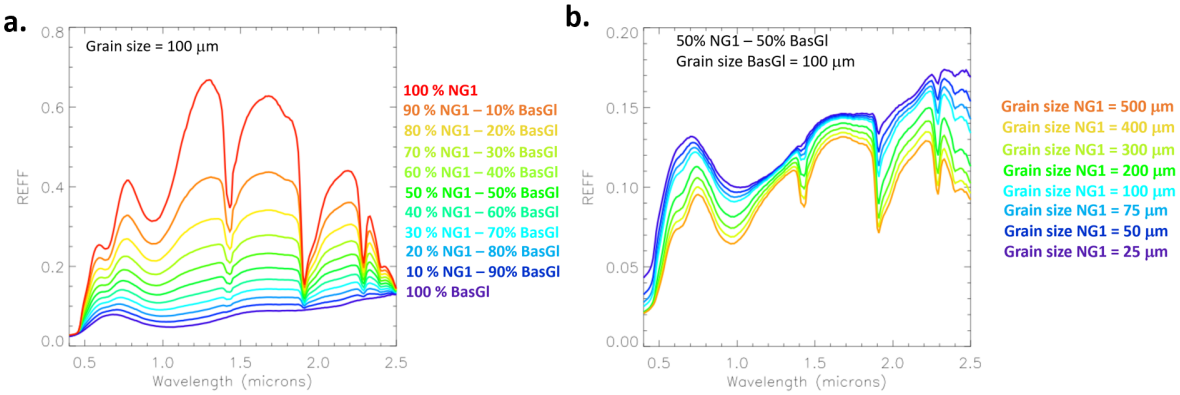

Figure 4: *(a) Evolution of the reflectance spectrum of a mixture made of nontronite and basaltic glass for different fractions. Grain diameter for both endmembers is set at 100 microns. (b) Evolution of the reflectance spectrum of a 50/50% mixture made of nontronite and basaltic glass for different grain sizes of the nontronite endmember. Grain diameter for basaltic glass is set at 100 microns.*

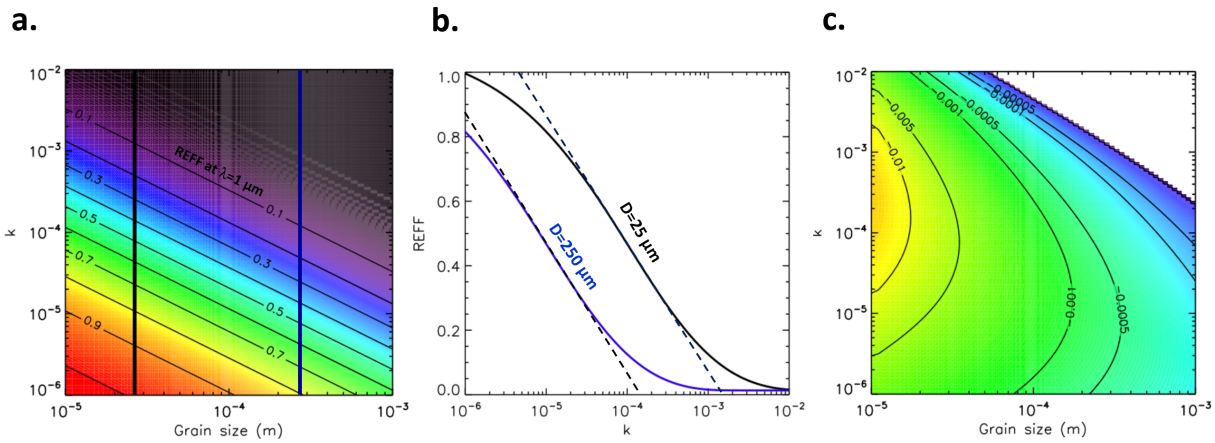

Figure 5: *(a) Evolution of the reflectance factor for a granular sample with the grain size (x-axis) and imaginary part of the optical constant k (y-axis). n is set to 1.5 here, the wavelength is 1 µm. (b) Vertical cross-sections displaying the evolution of the reflectance factor with k (cases where the grain diameters are 25 and 250 µm). Dashed lines are added to highlight the shape of the curves and their inflection point. (c) Sensitivity of the reflectance factor shown in (a) to an increase of the grain size (in REFF unit /µm). The right top corner (in white) corresponds to the weak-surface-scattering region (no sensitivity of REFF to the grain size).*

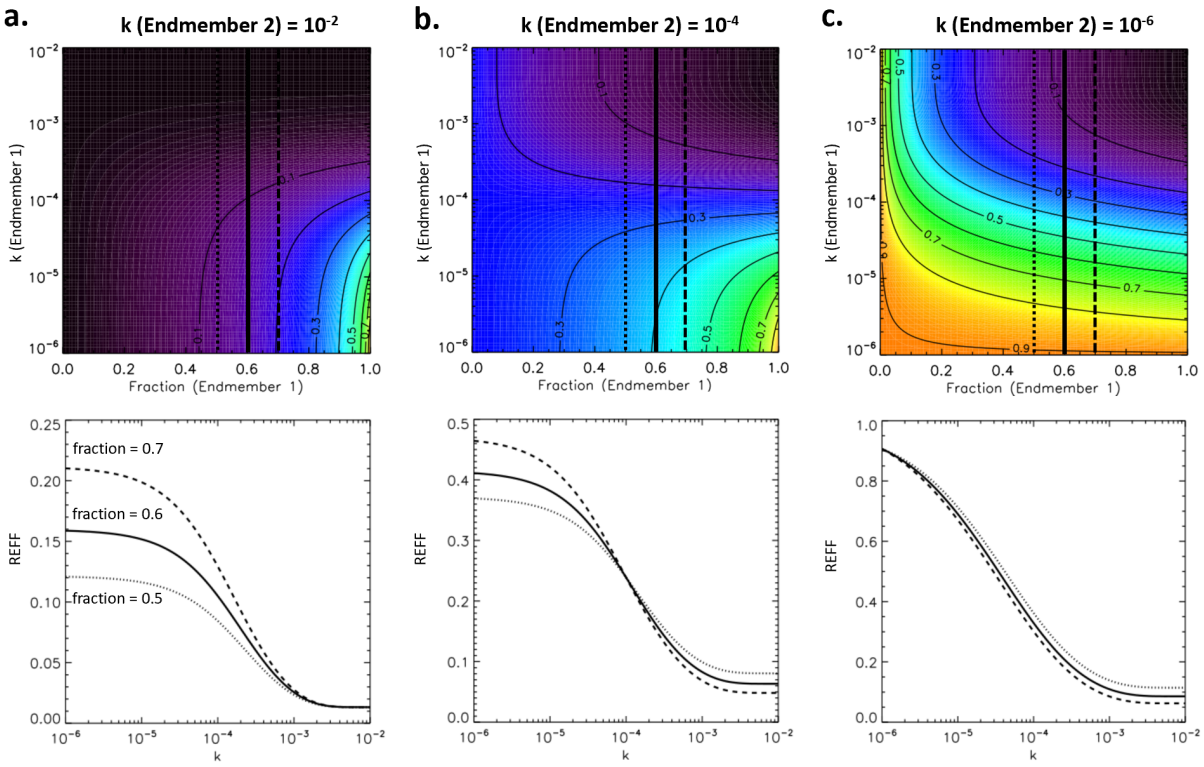

Figure 6: *First row - Evolution of the reflectance factor for a mixture of two endmembers with the fraction and imaginary part of the optical constant k of Endmember 1 for three cases of imaginary part of the optical constant of Endmember 2: (a) $k = 10^{-2}$, (b) $k = 10^{-4}$, (c) $k = 10^{-6}$. n is set to 1.5 here, the wavelength is 1 µm and the grain diameter of both endmembers is 100 µm. Second row - Vertical cross-sections displaying the evolution of the reflectance factor with k for three fractions of Endmember 1: 0.5, 0.6 and 0.7.*

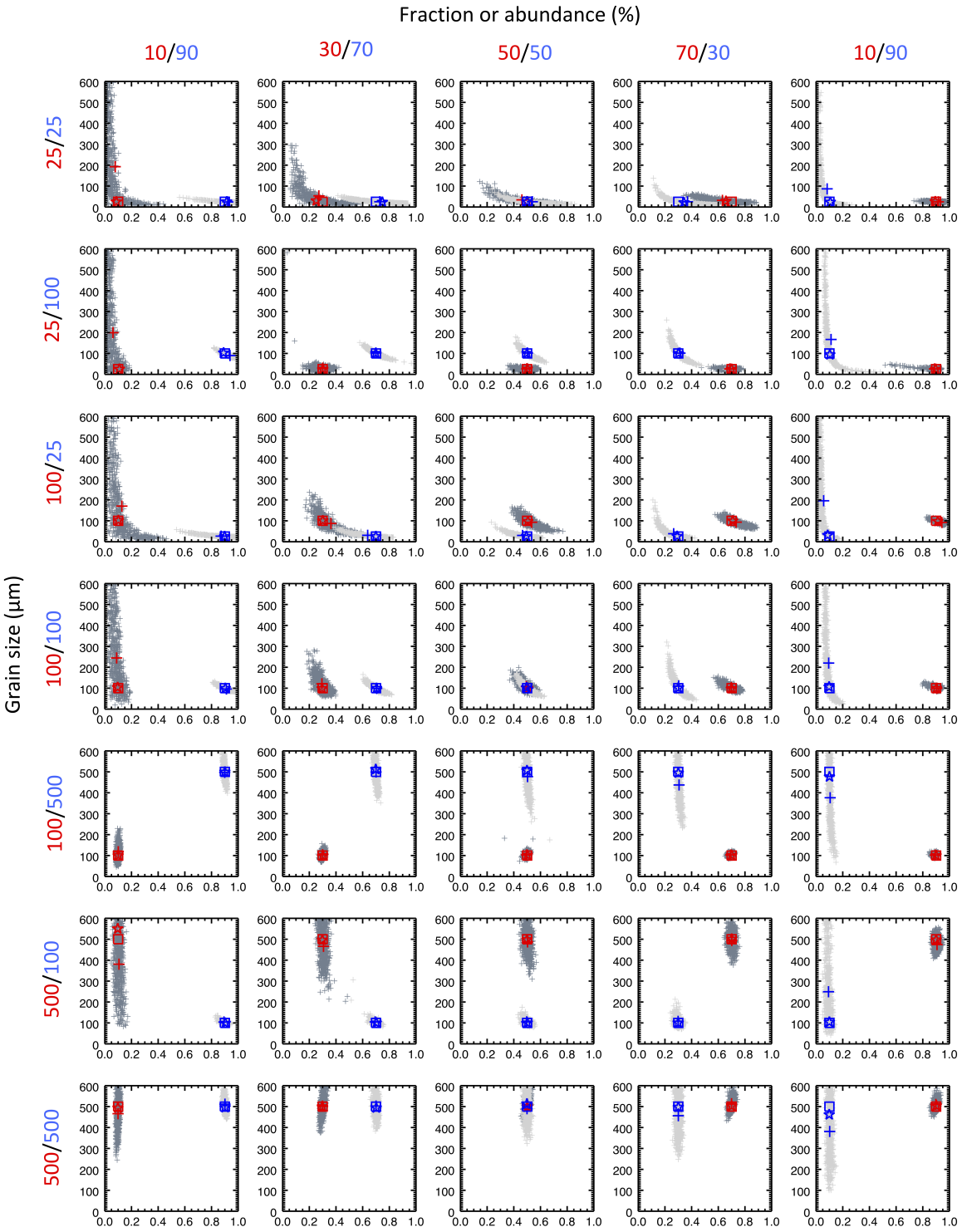

Figure 7: *Inversion results obtained on a mixture of nontronite (NG1, Endmember 1) and basaltic glass (BasGl, Endmember 2) with the Hapke model, assuming a data uncertainty of 20%. From left to right: 10/90%, 30/70%, 50/50%, 70/30%, 90/10% fractions. From top to bottom: 25/25 µm, 25/100 µm, 100/25 µm, 100/100 µm, 100/500 µm, 500/100 µm, 500/500 µm grain diameters. Endmember 1 solutions: dark gray crosses; endmember 2 solutions: light gray crosses. References: squares (red for endmember 1 and blue for endmember 2); distribution likelihood maximum: stars (red for endmember 1 and blue for endmember 2); distribution mean: bold crosses (red for endmember 1 and blue for endmember 2).*

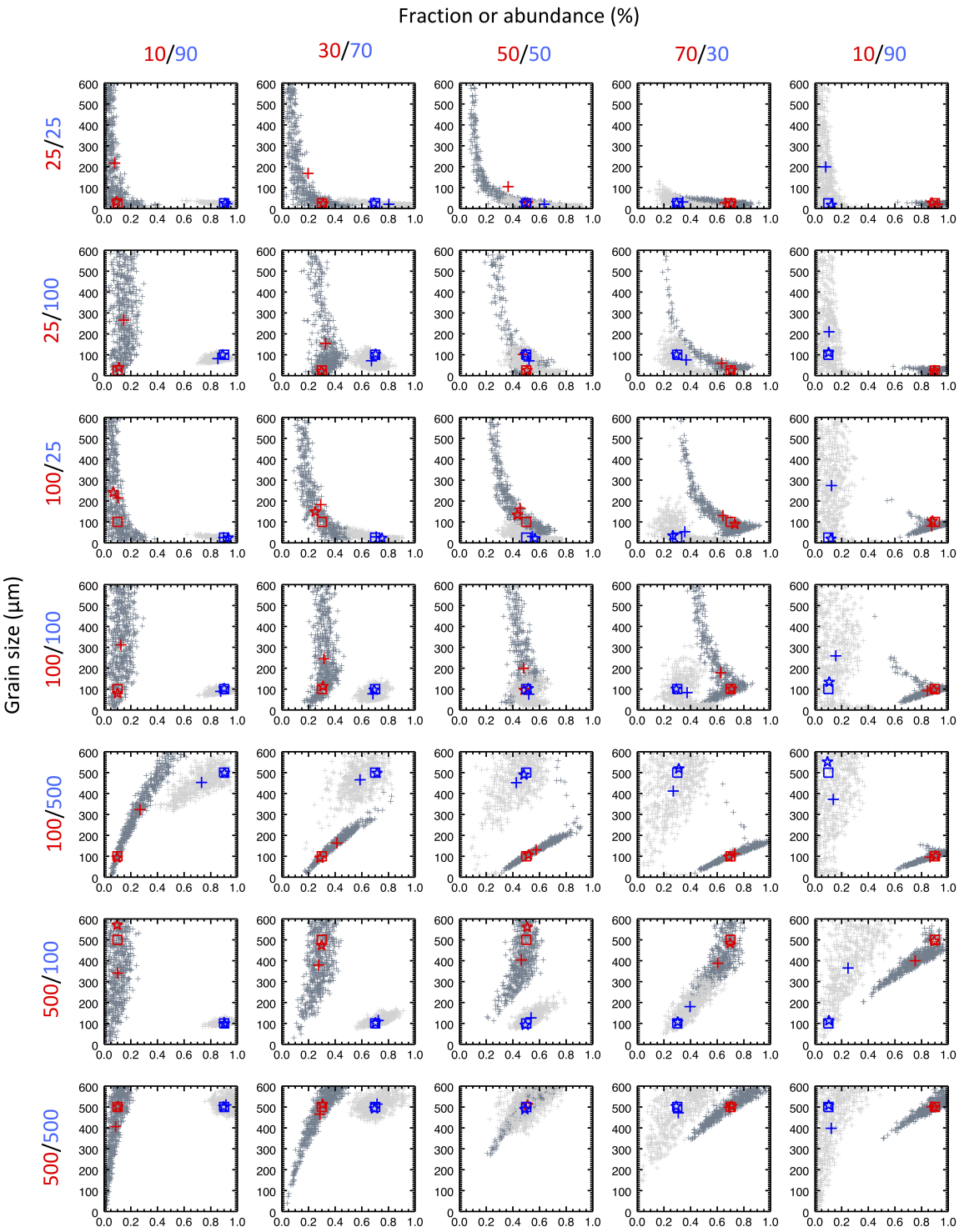

Figure 8: *Same as Fig.7 for a mixture of basalt (BAS, Endmember 1) and basaltic glass (BasGl, Endmember 2). Endmember 1 solutions: dark gray crosses; endmember 2 solutions: light gray crosses. References: squares (red for endmember 1 and blue for endmember 2); distribution likelihood maximum: stars (red for endmember 1 and blue for endmember 2); distribution mean: bold crosses (red for endmember 1 and blue for endmember 2).*

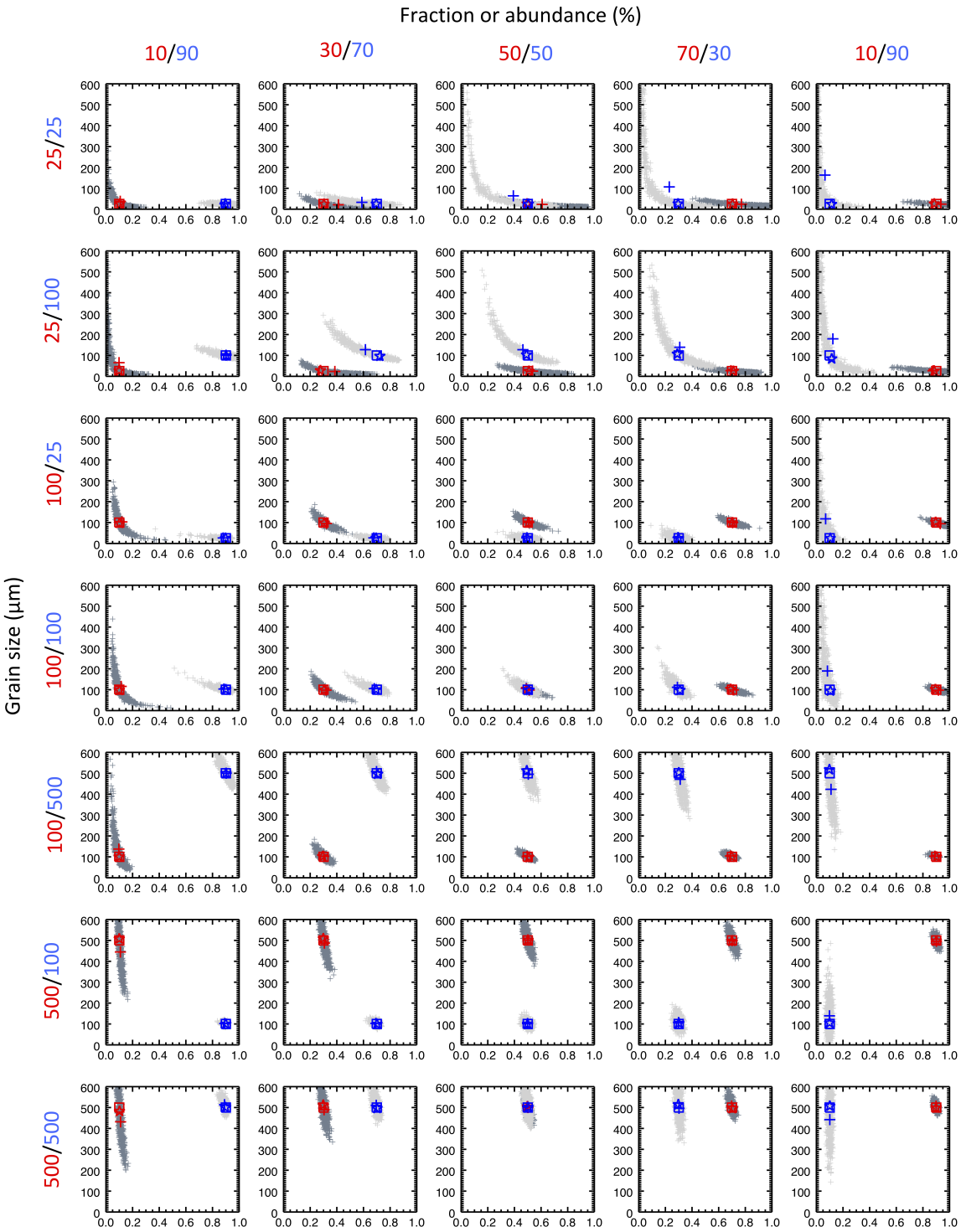

Figure 9: *Same as Fig.7 for a mixture of nontronite (NG1, Endmember 1) and olivine/forsterite (OLV, Endmember 2). Endmember 1 solutions: dark gray crosses; endmember 2 solutions: light gray crosses. References: squares (red for endmember 1 and blue for endmember 2); distribution likelihood maximum: stars (red for endmember 1 and blue for endmember 2); distribution mean: bold crosses (red for endmember 1 and blue for endmember 2).*

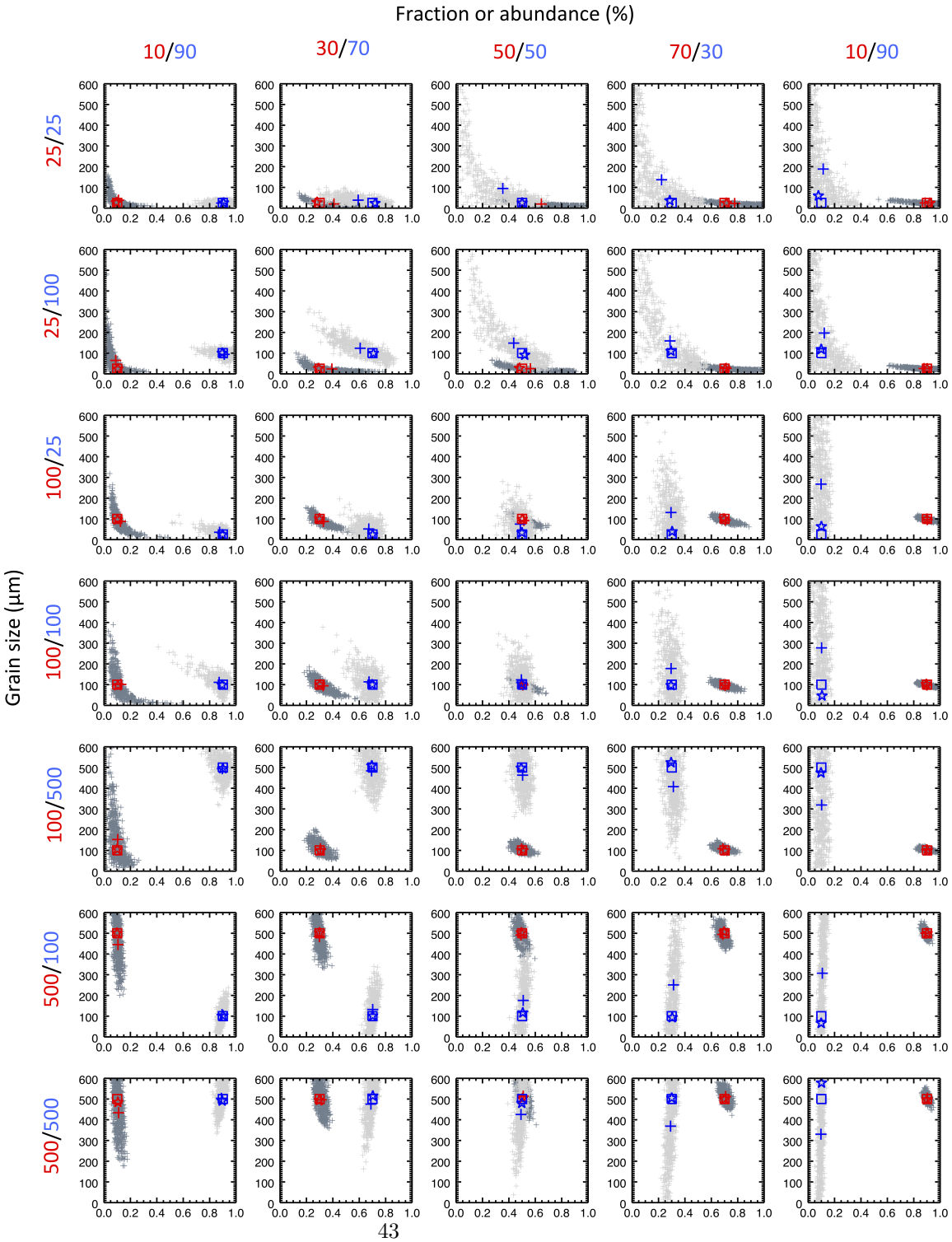

Figure 10: *Same as Fig.7 for a mixture of nontronite (NG1, Endmember 1) and magnesite (MGC, Endmember 2). Endmember 1 solutions: dark gray crosses; endmember 2 solutions: light gray crosses. References: squares (red for endmember 1 and blue for endmember 2); distribution likelihood maximum: stars (red for endmember 1 and blue for endmember 2); distribution mean: bold crosses (red for endmember 1 and blue for endmember 2).*

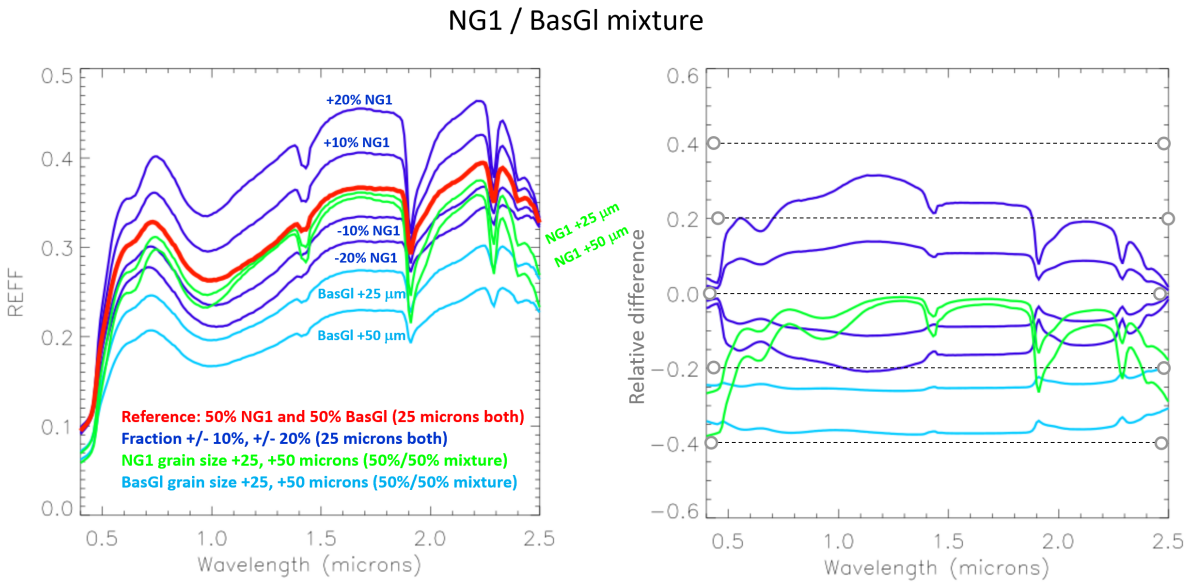

Figure 11: *Evaluation of the spectrum sensitivity for a 50%/50% NG1/BasGl mixture (grain diameter of 25 microns for both endmembers). Reflectance spectra are displayed on the left, while the relative difference with regards to the reference spectrum is displayed on the right. Grain size affects the spectrum to a larger extent with peak values above 0.2 in all displayed cases. Fraction only affects the spectrum under 0.2, except for the case with 70% NG1. For the latter, Fig.7 shows that the reflectance factor increase (resulting from an increase of the NG1 fraction) is actually compensated by an increase of the BasGl grain size.*

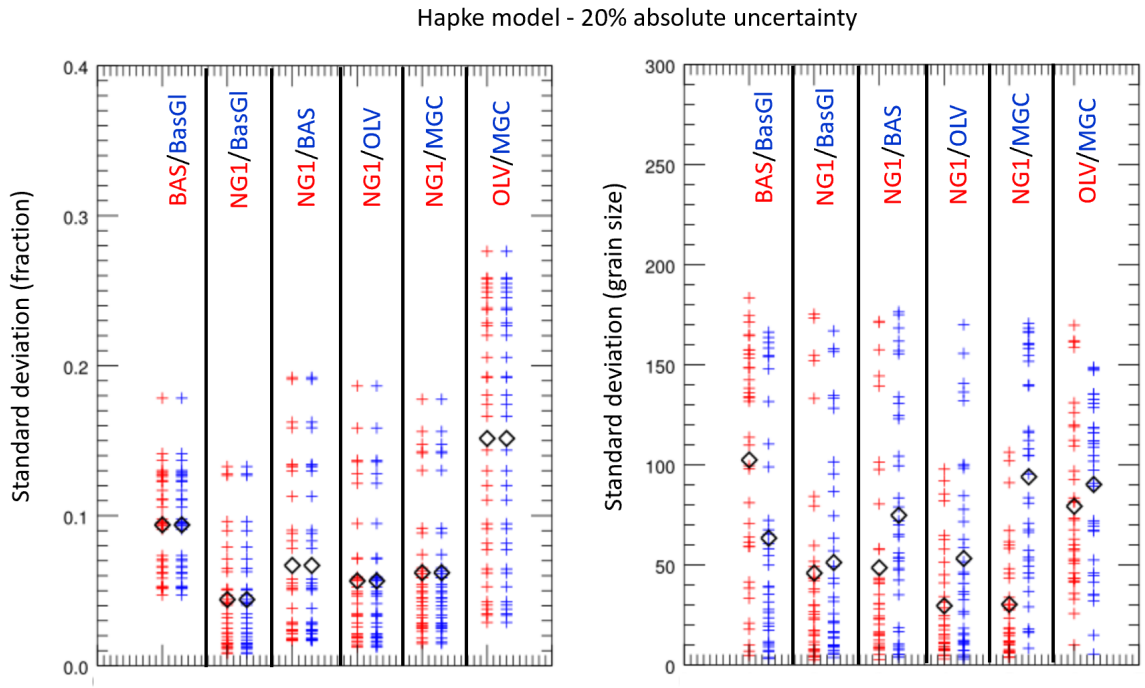

Figure 12: *Standard deviation of the fraction (left) and grain diameter (right) calculated from the inversion results using the Hapke model with a data uncertainty of 20%. Endmember 1: red crosses; endmember 2: blue crosses. Black crystals represent the average standard deviation over all tested cases for each couple of endmembers.*

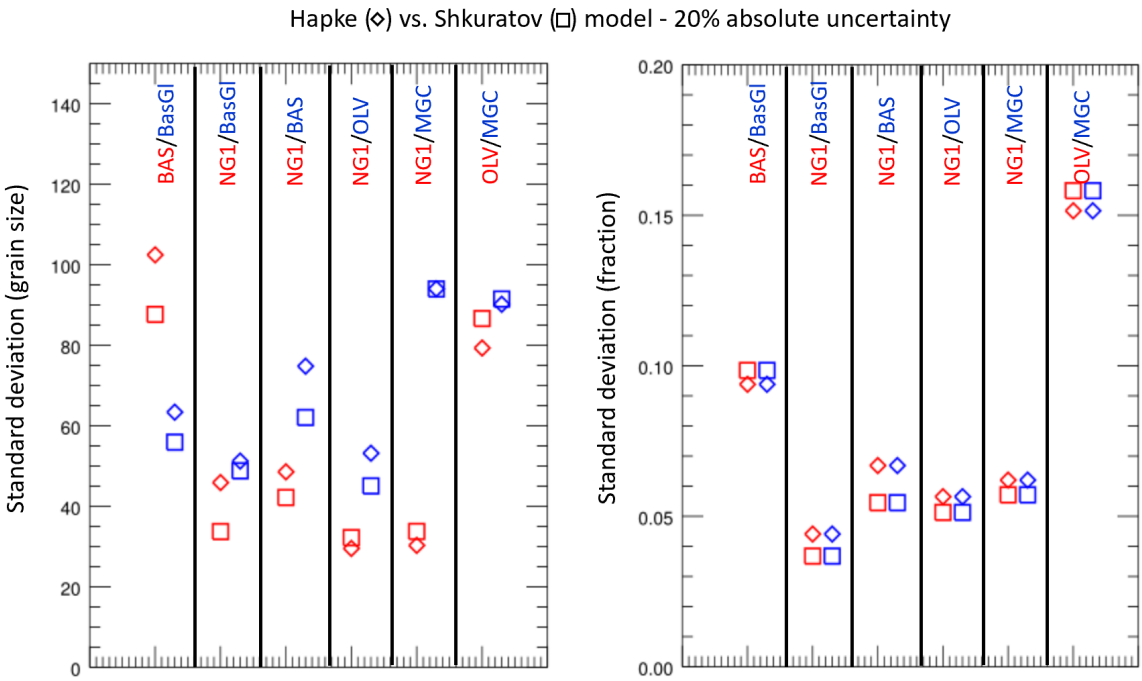

Figure 13: *Comparison of the average standard deviations calculated from the inversion results for the two models (Hapke: crystals, and Shkuratov: squares) in the case of a data uncertainty of 20%. Endmember 1: red; endmember 2: blue.*

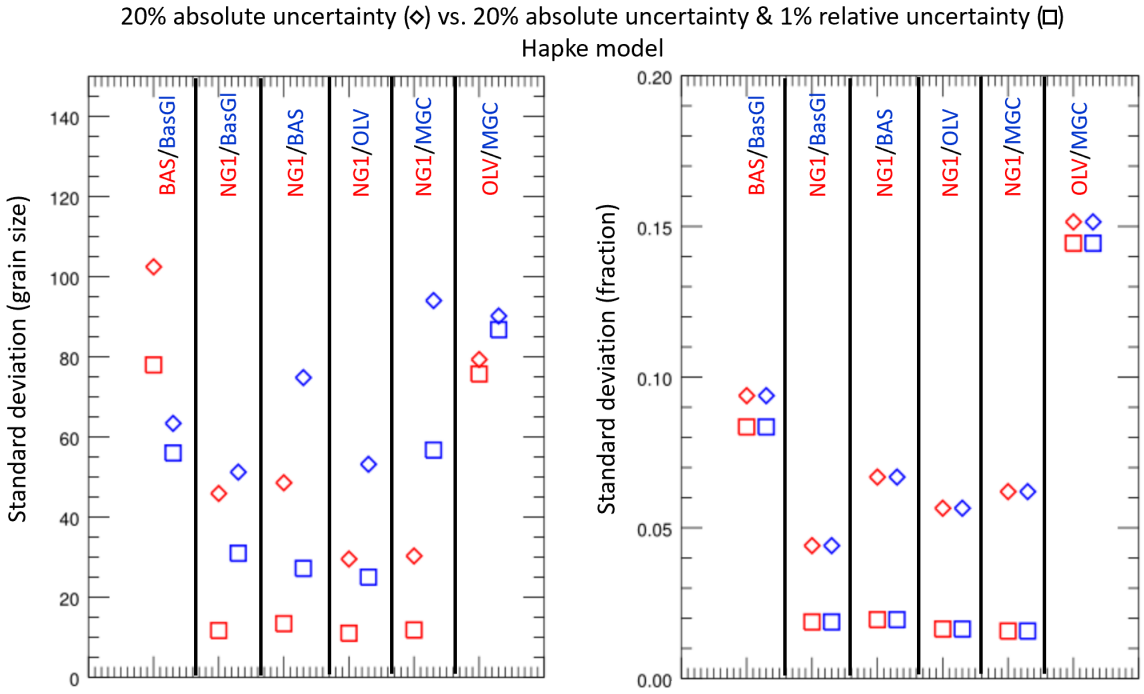

Figure 14: *Comparison of the average standard deviations (fraction on the left, grain size on the right) calculated from the inversion results with the Hapke model in the case of a data uncertainty of 20% (crystals) and in the case where an uncertainty of 1% from 1 spectral channel to the next is also taken into account (squares). Endmember 1 (red), endmember 2 (blue).*

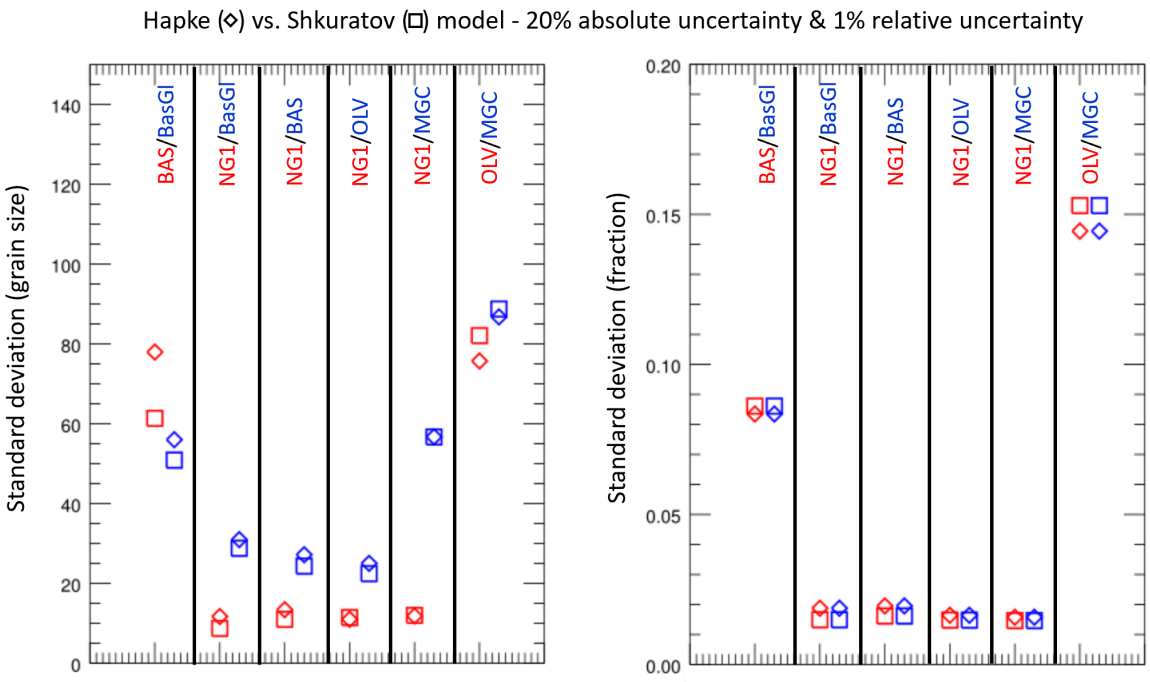

Figure 15: *Same as Fig.13 in the case of a data uncertainty of 20% and 1% from 1 spectral channel to the next. Endmember 1 (red), endmember 2 (blue).*

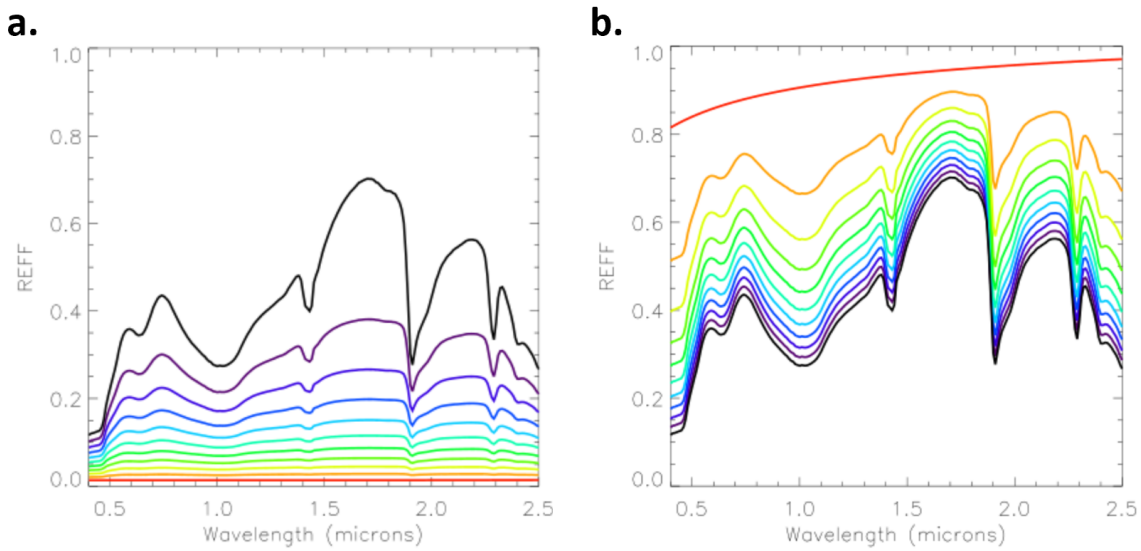

Figure 16: *(a) Reflectance spectra of a mixture of nontronite (NG1), olivine/forsterite (OLV) and a 3rd endmember with the following optical constants:* $1.5+10^{-2}i$*. Fractions of NG1 and OLV are equal. The fraction of the 3rd endmember increases from 0% (black) to 100% (red) (10% steps). Grain diameters of all three endmembers are set to 100 microns. (b) Reflectance spectra of a mixture of nontronite (NG1), olivine/forsterite (OLV) and a 3rd endmember with the following optical constants:* $1.5 + 10^{-6}i$*.*

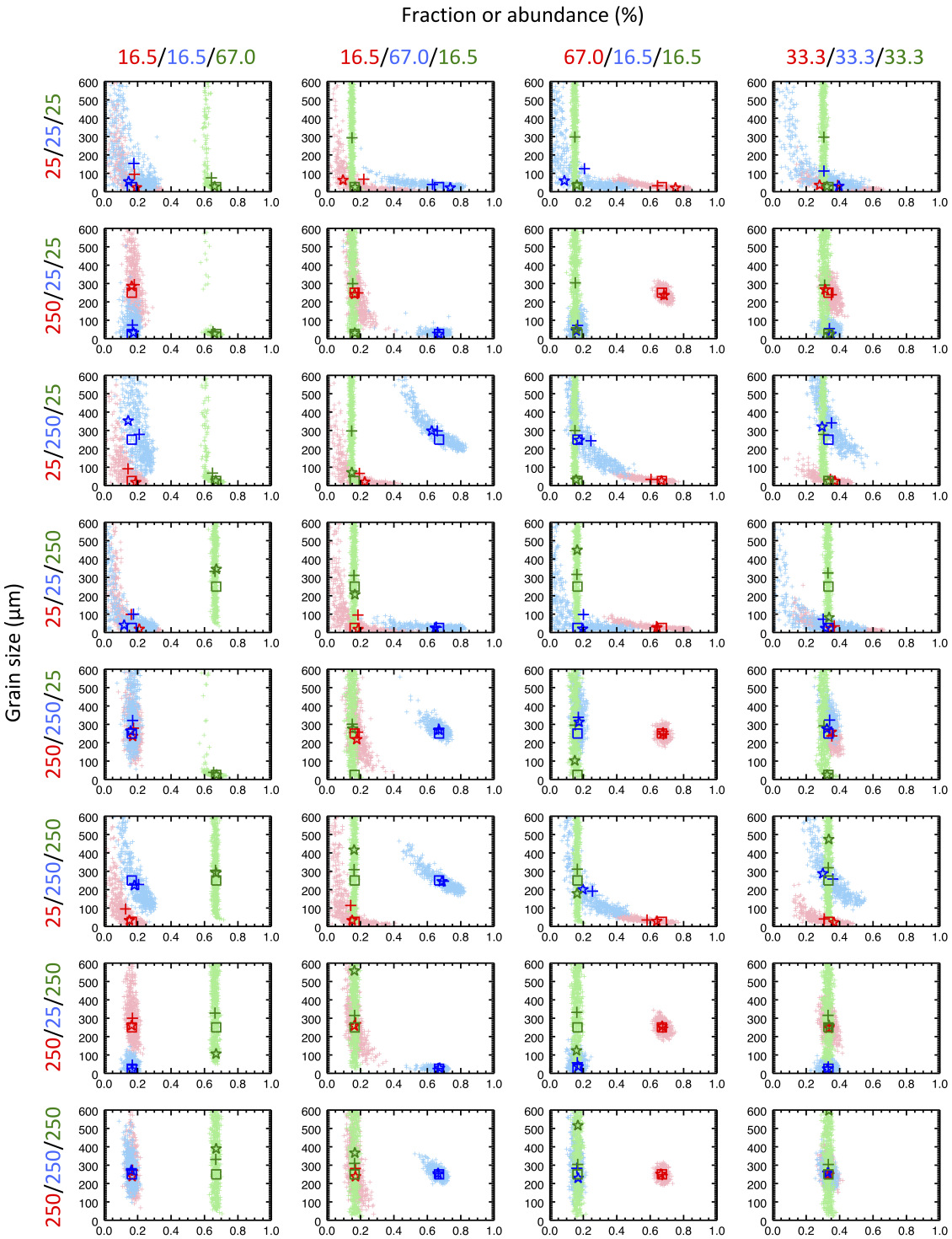

Figure 17: *Inversion results obtained on a mixture of nontronite (NG1), olivine/forsterite (OLV) and Compound 3 (with $n = 1.5$ and $k = 10^{-2}$) with the Hapke model, assuming a data uncertainty of 20%. From left to right: 16.5/16.5/67.0%, 16.5/67.0/16.5%, 67.0/16.5/16.5%, 33.3/33.3/33.3% fractions. From top to bottom: 25/25/25 µm, 250/25/25 µm, 25/250/25 µm, 25/25/250 µm, 250/250/25 µm, 25/250/250 µm, 250/25/250 µm, 250/250/250 µm grain diameters. Endmember 1 solutions: light red crosses; endmember 2 solutions: light blue crosses ; endmember 3 solutions: light green crosses. References: squares; distribution likelihood maximum: stars; distribution mean: bold crosses. Endmember 1 (red), Endmember 2 (blue), endmember 3 (green).*

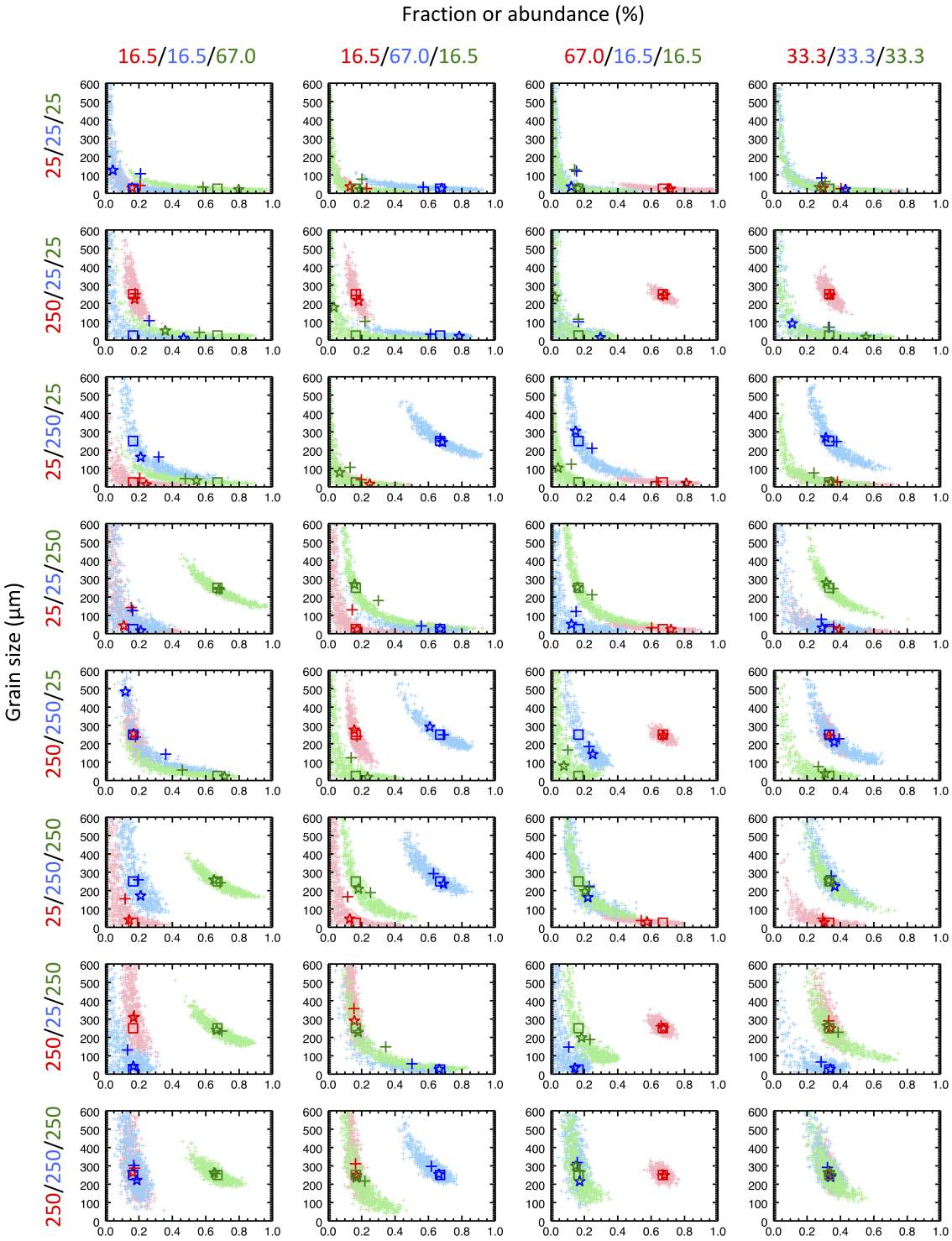

Figure 18: *Inversion results obtained on a mixture of nontronite (NG1), olivine/forsterite (OLV) and Compound 3 (with $n = 1.5$ and $k = 10^{-4}$) with Hapke model, assuming a data uncertainty of 20%. From left to right: 16.5/16.5/67.0%, 16.5/67.0/16.5%, 67.0/16.5/16.5%, 33.3/33.3/33.3% fractions. From top to bottom: 25/25/25 µm, 250/25/25 µm, 25/250/25 µm, 25/25/250 µm, 250/250/25 µm, 25/250/250 µm, 250/25/250 µm, 250/250/250 µm grain diameters. Endmember 1 solutions: light red crosses; endmember 2 solutions: light blue crosses ; endmember 3 solutions: light green crosses. References: squares; distribution likelihood maximum: stars; distribution mean: bold crosses. Endmember 1 (red), Endmember 2 (blue), endmember 3 (green).*

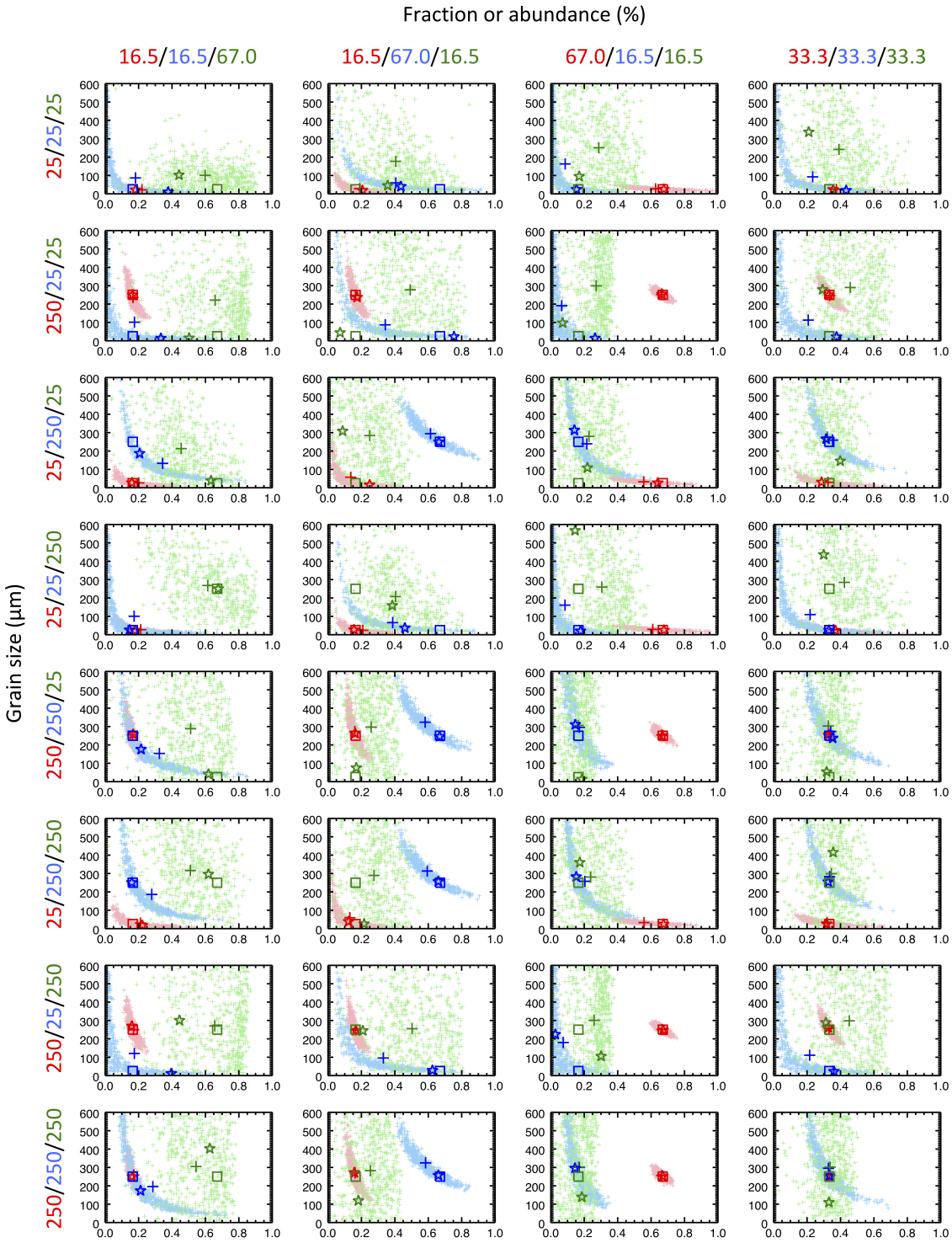

Figure 19: *Inversion results obtained on a mixture of nontronite (NG1), olivine/forsterite (OLV) and Compound 3 (with $n = 1.5$ and $k = 10^{-6}$) with Hapke model, assuming a data uncertainty of 20%. From left to right: 16.5/16.5/67.0%, 16.5/67.0/16.5%, 67.0/16.5/16.5%, 33.3/33.3/33.3% fractions. From top to bottom: 25/25/25 µm, 250/25/25 µm, 25/250/25 µm, 25/25/250 µm, 250/250/25 µm, 25/250/250 µm, 250/25/250 µm, 250/250/250 µm grain diameters. Endmember 1 solutions: light red crosses; endmember 2 solutions: light blue crosses ; endmember 3 solutions: light green crosses. References: squares; distribution likelihood maximum: stars; distribution mean: bold crosses. Endmember 1 (red), Endmember 2 (blue), endmember 3 (green).*

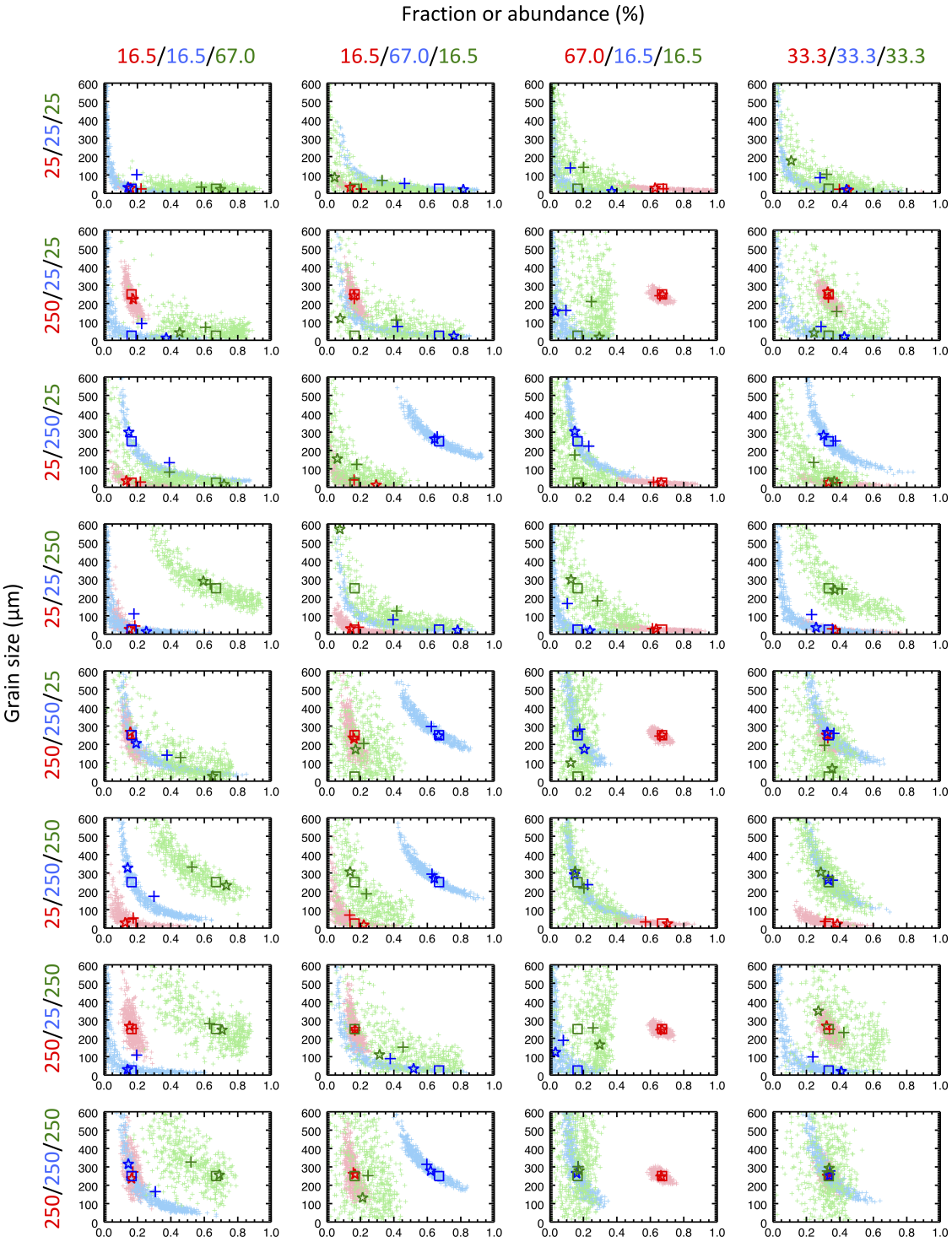

Figure 20: *Inversion results obtained on a mixture of nontronite (NG1), olivine/forsterite (OLV) and magnesite (MGC) with Hapke model, assuming a data uncertainty of 20%. From left to right: 16.5/16.5/67.0%, 16.5/67.0/16.5%, 67.0/16.5/16.5%, 33.3/33.3/33.3% fractions. From top to bottom: 25/25/25 µm, 250/25/25 µm, 25/250/25 µm, 25/25/250 µm, 250/250/25 µm, 25/250/250 µm, 250/25/250 µm, 250/250/250 µm grain diameters. Endmember 1 solutions: light red crosses; endmember 2 solutions: light blue crosses ; endmember 3 solutions: light green crosses. References: squares; distribution likelihood maximum: stars; distribution mean: bold crosses. Endmember 1 (red), Endmember 2 (blue), endmember 3 (green).*

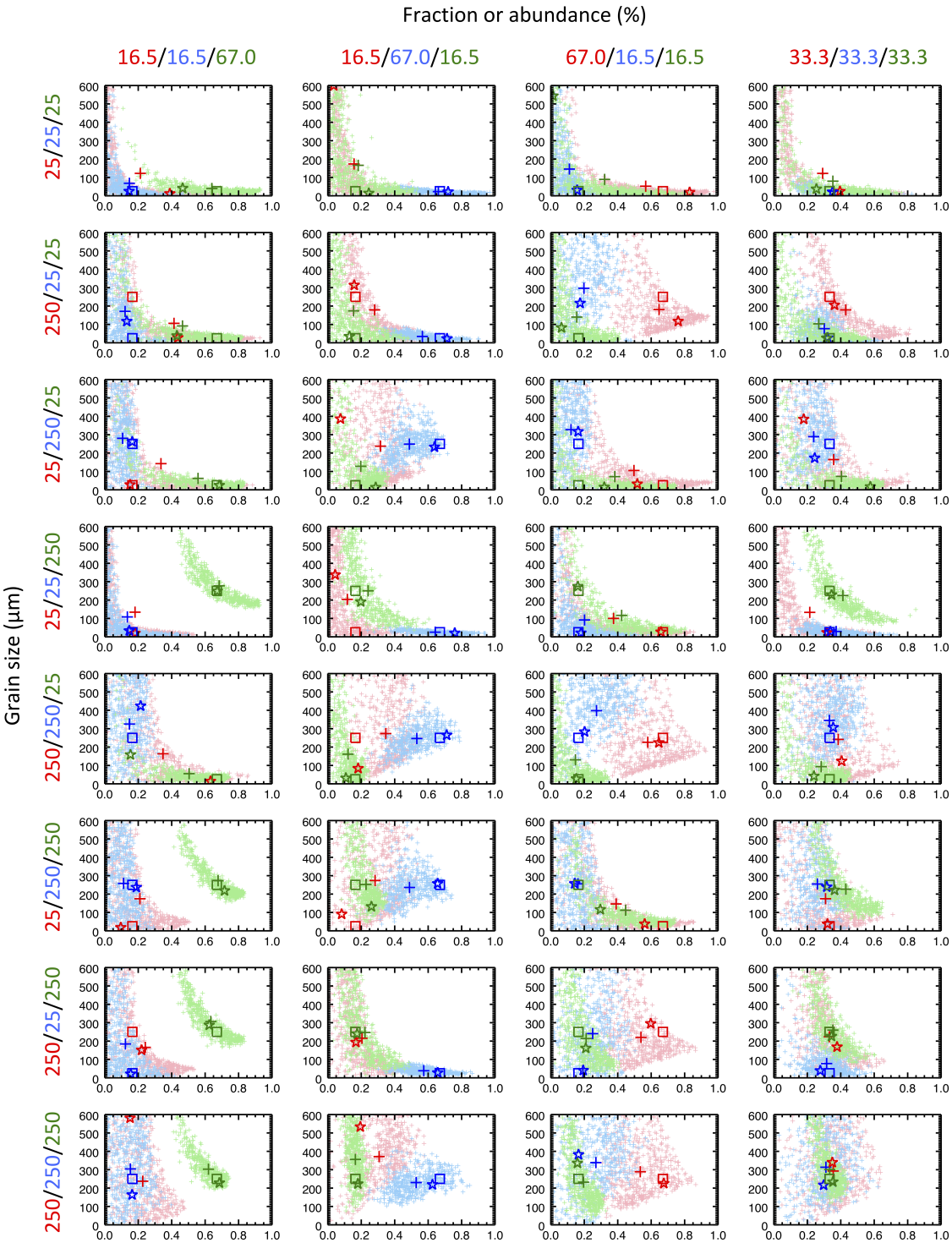

Figure 21: *Inversion results obtained on a mixture of basalt (BAS), basaltic glass (BasGl) and olivine/forsterite (OLV) with Hapke model, assuming a data uncertainty of 20%. From left to right: 16.5/16.5/67.0%, 16.5/67.0/16.5%, 67.0/16.5/16.5%, 33.3/33.3/33.3% fractions. From top to bottom: 25/25/25 µm, 250/25/25 µm, 25/250/25 µm, 25/25/250 µm, 250/250/25 µm, 25/250/250 µm, 250/25/250 µm, 250/250/250 µm grain diameters. Endmember 1 solutions: light red crosses; endmember 2 solutions: light blue crosses ; endmember 3 solutions: light green crosses. References: squares; distribution likelihood maximum: stars; distribution mean: bold crosses. Endmember 1 (red), Endmember 2 (blue), endmember 3 (green).*

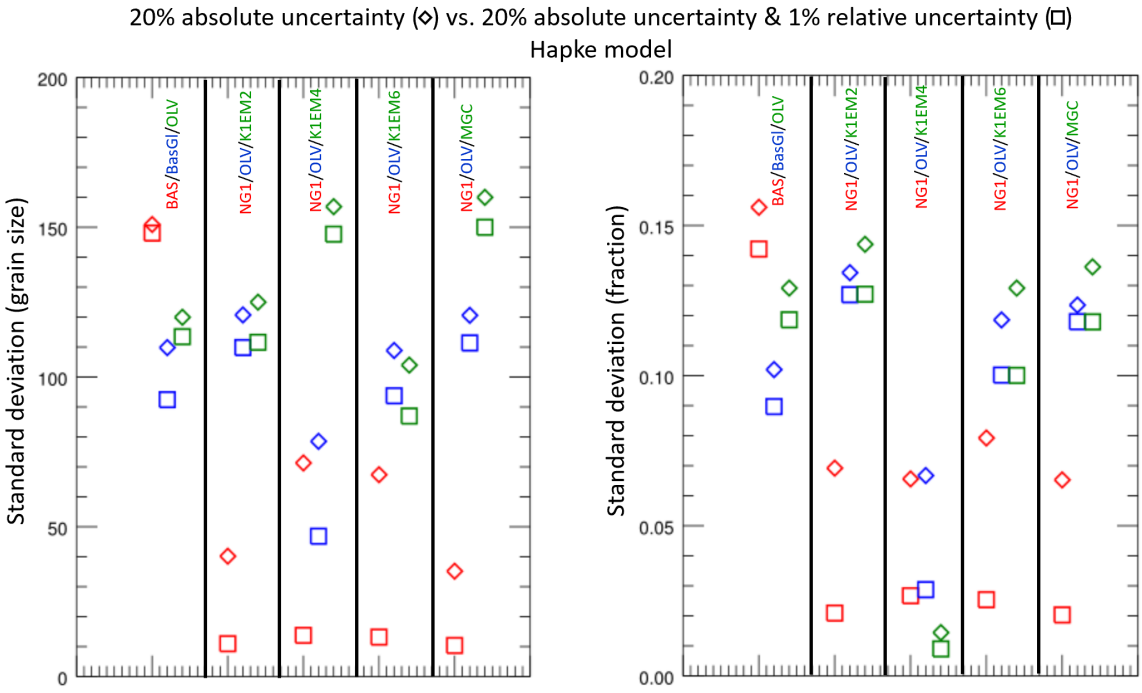

Figure 22: *Comparison of the average standard deviations (fraction on the right, grain size on the left) calculated from the inversion results in the case of a data uncertainty of 20% (crystals) and in the case where an uncertainty of 1% from 1 spectral channel to the next is also taken into account (squares). Endmember 1 (red), endmember 2 (blue) and endmember 3 (green).*

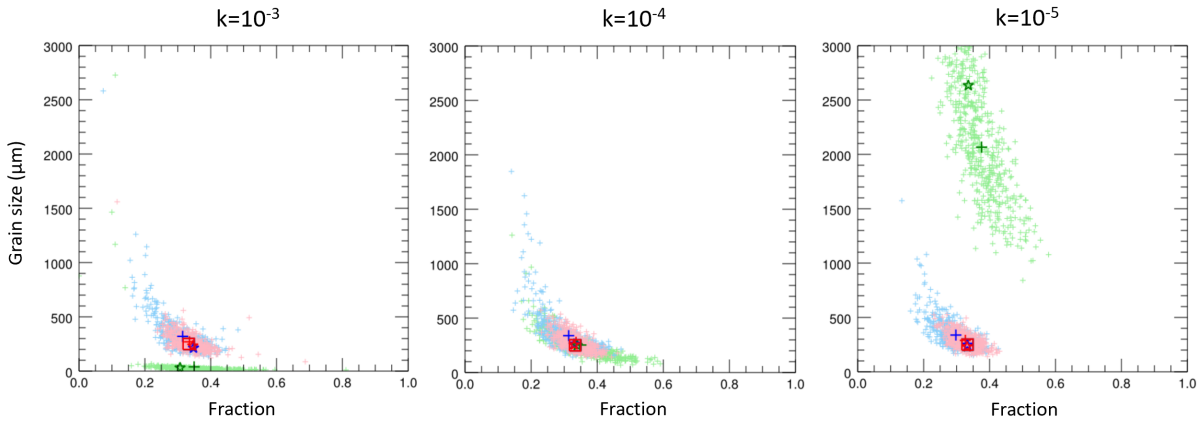

Figure 23: *Inversion results obtained on a mixture of nontronite (NG1) (Endmember 1, in red), olivine/forsterite (OLV) (Endmember 2, in blue) and a third compound (Endmember 3, in green) having the following properties:* $n = 1.5$ *and* $k = 10^{-4}$ *(i.e. no spectral features are assumed for this test). Grain diameters of Endmembers 1, 2 and 3 are set to 250 microns. We assumed here a data uncertainty of 20% (the Hapke model is used). The inversion is made by considering here the Endmember 3 as unknown and testing different optical properties for this compound:* $k = 10^{-3}$ *(left),* $k = 10^{-4}$ *(middle),* $k = 10^{-5}$ *(right). Inversion results are represented by small crosses, the reference by a square, the distribution likelihood maximum by a star and the distribution mean by a cross.*

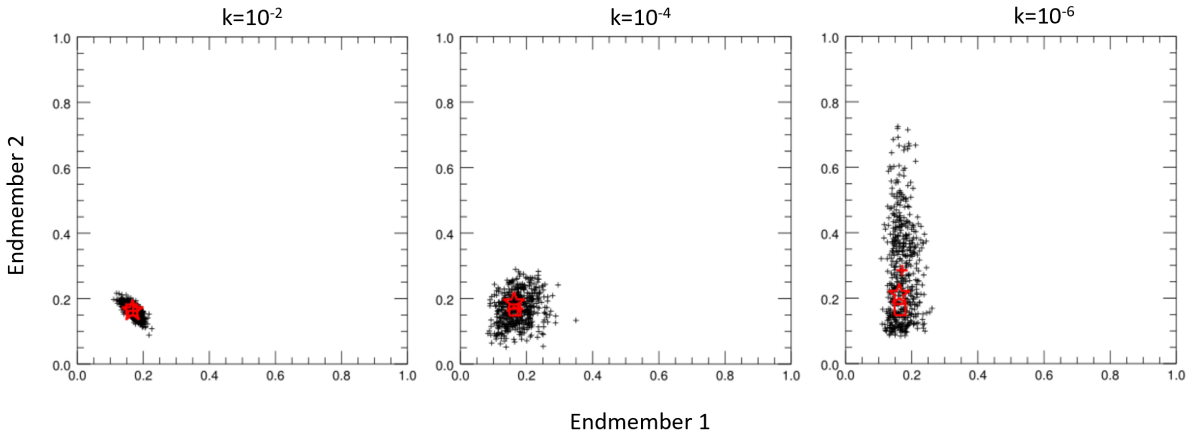

Figure 24: *Inversion results (fraction of Endmember 1 and Endmember 2) obtained on a mixture of 16.6% of nontronite (NG1) (Endmember 1), 16.6% of olivine/forsterite (OLV) (Endmember 2) and 66.7% of a third compound (Endmember 3) with the following properties:* $n = 1.5$ *and* $k = 10^{-2}$ *(left),* $k = 10^{-4}$ *(center),* $k = 10^{-6}$ *(right). Grain diameters of the three endmembers are set to 250 microns. We assumed a data uncertainty of 20% and the Hapke model is used here. Inversion results are represented by black crosses, the reference by a red square, the distribution likelihood maximum by a red star and the distribution mean by a red cross.*

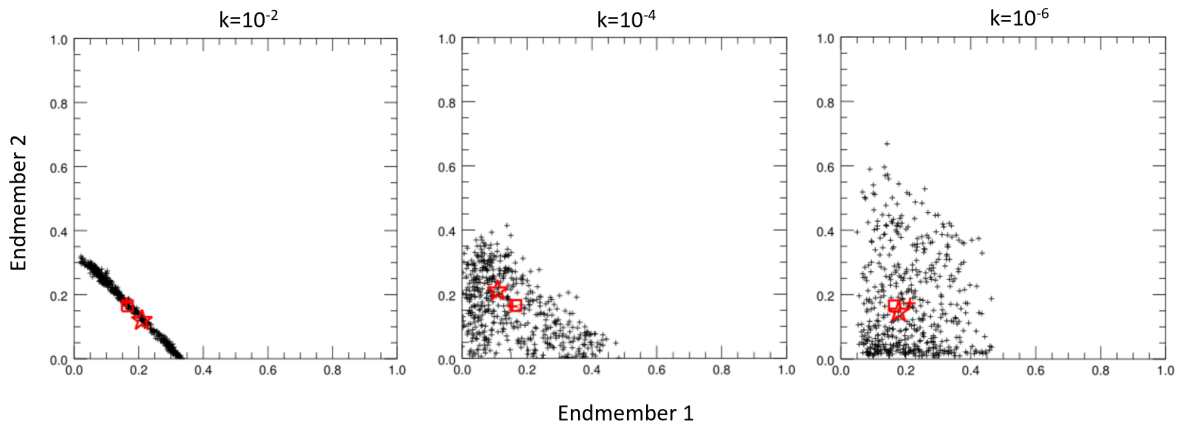

Figure 25: *Same as Fig.24, with the grain diameters of Endmembers 1 and 2 set to 25 microns (x10 smaller) while the grain diameter of Endmember 3 remains at 250 microns.*

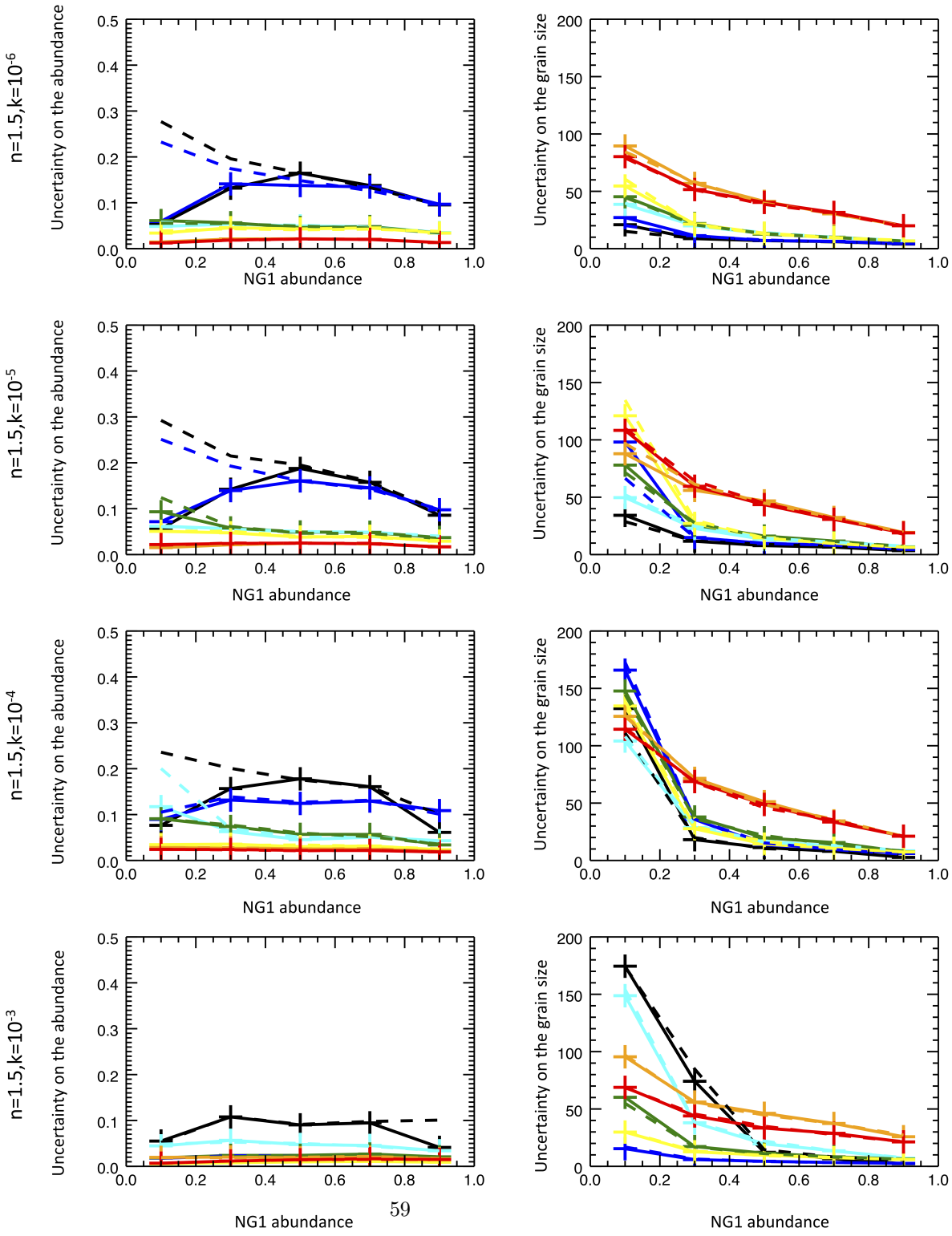

Figure 26: *Uncertainties (1σ) on the nontronite (NG1) obtained when inverting the reflectance spectra of mixtures made of nontronite (Endmember 1) and a second endmember with the various properties. Grain diameters for the different endmembers are as follows: 25µm for Endmembers 1 and 2 (black), 25µm for Endmember 1 and 100µm for Endmember 2 (blue), 100µm for Endmember 1 and 25µm for Endmember 2 (cyan), 100µm for Endmembers 1 and 2 (green), 100µm for Endmember 1 and 500µm for Endmember 2 (yellow), 500µm for Endmember 1 and 100µm for Endmember 2 (orange), 500µm for Endmembers 1 and 2 (red). The continuous lines correspond to the case where the grain size is tested over the 10-600µm range, while the dashed lines correspond to the 1-600µm range. This highlights the boundary effects present when the grain sizes are small as the second endmember is featureless. The Hapke model is used and a 20% uncertainty on the reflectance factor is assumed.*

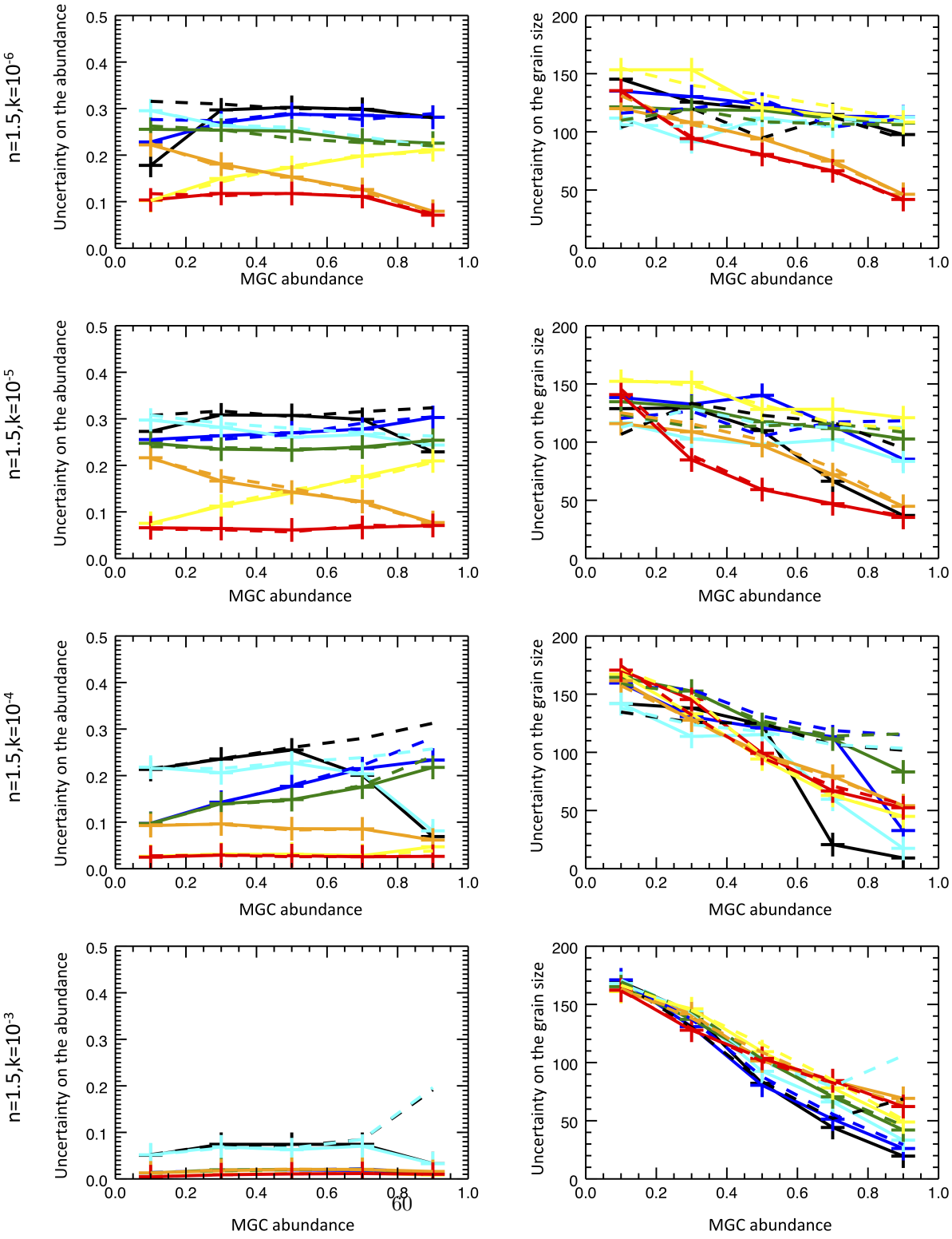

Figure 27: *Same as Figure 26 for the magnesite (MGC).*